6

SENSORS AND TECHNIQUES FOR OBSERVING THE BOUNDARY LAYER

Sensors used for boundary layer measurements fall into two broad categories: in situ sensors that can be mounted on the ground, on masts, towers, tethered balloons, free balloons, or aircraft; and remote sensors, ground-based or aircraft-mounted, that infer atmospheric properties through their effects on acoustic, microwave, and optical signals propagating through the air. In situ sensors are the traditional instruments of choice for surface and lower boundary layer studies, being the only ones capable of the accuracy and resolution needed for quantitative work. A major portion of this chapter will therefore be devoted to discussions of their characteristics. Remote sensors have the advantage of increased range and spatial scanning capability, but the constraints on minimum range and spatial resolution limit their usefulness for surface layer measurements. Used in combination, however, the two types of sensors provide a more complete description of the flow field being studied than either of the two can provide separately. New remote sensors with shorter minimum ranges and finer range resolutions are now becoming available for boundary layer applications. A brief discussion of such devices is also included in this chapter.

The variables of greatest interest to boundary layer meteorologists are wind speed, temperature, humidity, and the fluxes of momentum, heat, mass, and radiant energy. Given suitable fast-response measurements of wind velocity and scalar fluctuations, we can calculate the eddy fluxes directly from the products of their fluctuating components (e.g., $\overline{u'w'}, \overline{w'\theta'}$) as explained in Chapter 1. If only the gradients of their means are available, however, then over a flat homogeneous surface the fluxes may be inferred from the Monin-Obukhov relationships of Chapters 1 and 3. Practical methods for doing that are described in many texts; see, for example, Monteith (1975, 1976). (Those simple relationships do not hold, as we know, under advective conditions, in plant canopies, and over hills.) There are also sensors in use that measure surface and near-surface fluxes directly, such as the drag plate (surface stress), the lysimeter (latent heat flux), flux plates (soil heat flux), and radiometers (radiant heat flux). We will discuss these and a few other types as well because of their application to studies of plant canopies.

We begin our survey with in situ sensors that measure the mean and fluctuating properties of air above the ground. The requirements for measurements of the two are different. Sensors for measuring the time-averaged properties of the flow require a high degree of absolute accuracy and long-term stability and should be able to provide good averages over periods 10 min and longer. Sensors for measuring the turbulent properties of the flow need a frequency response broad enough to cover all the eddy scales contributing to the process, but the accuracy need only be relative, that is, with respect to any arbitrary working mean. For measuring both means and fluctuations, the accuracy requirements are the same: ± 0.05 m s^{-1} for wind velocity, ± 0.05°C for temperature, and ± 0.05 mb for humidity. The response time for mean sensors can be as large as 1 min; but for fluctuation sensors it should be no longer than 0.1 s. These requirements are based on our present understanding of boundary layer structure over uniform terrain. In the case of technologies that are evolving (e.g., trace gas measurements), however, the accuracies and response times are what the state of the art can offer.

6.1 In situ sensors for profile measurements

6.1.1 *Mean wind sensors*

Cup anemometers, propeller anemometers, and vanes are the devices most commonly used to measure wind profiles. They are rugged, dependable, and relatively inexpensive. They depend on moving parts coming into dynamic equilibrium with the flow, so their response times are typically too long for turbulence work. But they are entirely adequate for mean profile measurements. Periodic calibrations and intercomparison checks are essential to ensure accuracy in the vertical gradient estimations.

Cup and vane systems are marketed in a variety of shapes and forms. The most common configuration is a three-cup anemometer and direction vane mounted side by side at the ends of a T-shaped horizontal boom. Both rotate on vertical axes, so they are separated horizontally to avoid mutual interference. The advantage of the cup anemometer is that it can accept winds from any direction. (Only the directions blocked by the wind vane and the supporting mast would be considered unfavorable.) For wind vanes with potentiometer systems that read vane position, the gap in the resistance element, typically a 10° sector, is often pointed in the direction of the mast to keep the number of unfavorable directions to a minimum. Starting speeds for cups are typically 0.5 m s^{-1}, and distance constant (63% recovery time converted to distance) is between 1.5 and 5 m. Properly designed cup anemometers can be calibrated in wind tunnels to an accuracy of $\pm 1\%$. There is a tendency in cup anemometers to overspeed, resulting partly from their nonlinear response to wind speeds (Fig. 6.1) and partly from sensitivity to the vertical component of the wind (see Fig. 6.2). Reports of overspeeding error range from 5% to 10%.

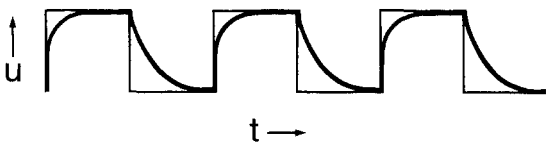

FIG. 6.1 Cup anemometer response (heavy curve) to square wave velocity function.

Propeller anemometers do not overspeed, but they operate dependably only when pointing directly into the wind. Propellers exhibit significant deviations from perfect cosine response (Fig. 6.3). When they are used in a fixed orthogonal configuration, corrections for deviation from cosine response have to be made based on an iterative approximation to the true wind direction (Horst, 1973). The measured wind components will otherwise be underestimated. A configuration well suited for profile measurements is the propeller-vane anemometer with its propeller mounted at the end of a vane with closely matched response characteristics. The vane keeps the propeller oriented into the wind. Propellers can be flat or helicoid. Two- and four-blade propellers are available, the former for high wind (>30 m s^{-1}). Accuracies and distance constants for propeller-vane anemometers are comparable to those of lightweight cup anemometers. Their calibrations should be checked in the wind tunnel; for most noncritical applications, periodic

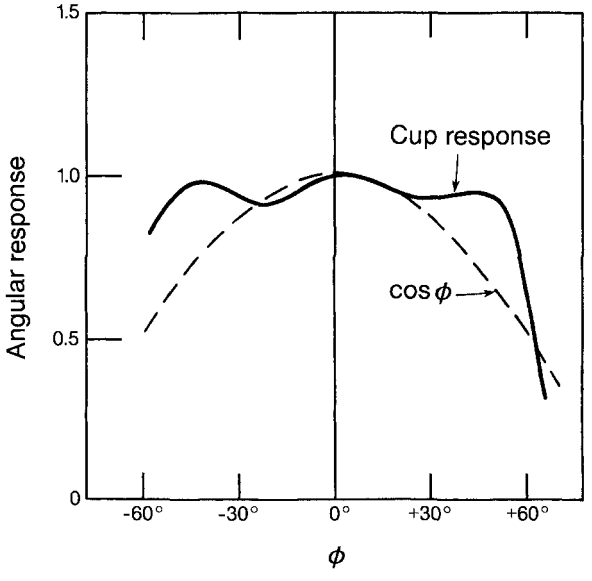

FIG. 6.2 Vertical velocity sensitivity in cup anemometers compared with ideal cosine response (after Busch et al., 1980). The inclination angle ϕ is defined positive for winds pointing downward.

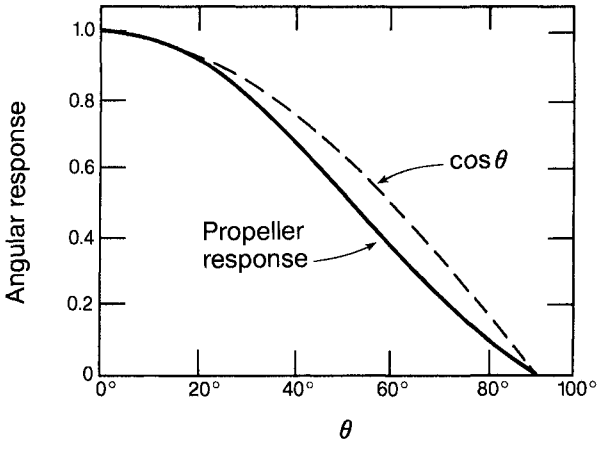

FIG. 6.3 Off-axis propeller response compared with ideal cosine response (after Busch et al., 1980). θ denotes the angle between the wind direction and the propeller axis.

calibration checks with a motor of known rotation rate (usually supplied by the manufacturer) are sufficient.

The optimum vertical spacing for wind profile measurement depends on the specific application. In the surface layer ($z \lesssim 50$ m), where the wind profile is roughly logarithmic, a vertical spacing that doubles with height (e.g., 1, 2, 4, 8, 16, 32 m) is often used. Above 50 m a fixed spacing is preferred, since the wind profile is no longer as sensitive to the presence of the ground below. For applications in which only one wind observation is required, as in surface wind networks, the World Meteorological Organization-recommended height is 10 m.

6.1.2 *Mean temperature sensors*

Temperature sensors most commonly used for measuring vertical gradients are platinum resistance thermometers, thermocouples, thermistors, and quartz thermometers. Accuracies of the order of 0.05°C and resolutions of 0.01°C can be achieved with careful calibration and attention to the design of leads, grounding, radiation shielding, and aspiration. The sensing elements are usually encapsulated in glass or metal for protection from atmospheric contamination and wear. The resulting increase in sensor mass and the attendant increase in time constant are not serious problems for mean profile measurements.

Platinum resistance thermometers are frequently used for both temperature and temperature difference measurements. The bridge circuit (see Fig. 6.4) is ideally suited for difference measurement. The bridge output V_o may be viewed as the difference between two voltage divider outputs:

$$V_o = \frac{E\alpha(T_2 - T_1)}{4(1 + \alpha T_a)}, \tag{6.1}$$

where E is the voltage across the bridge, α is the temperature coefficient of resistance (0.0039 at 0°C for platinum), T_1 and T_2 are the temperatures in degrees Celsius at the two elements, and T_a is the ambient temperature equal to $(T_1+T_2)/2$. The bridge sensitivity decreases with increasing T_a. For platinum, this amounts to a decrease of 12% over the range 0–30°C. Where long leads are involved, lead compensation should be provided to counterbalance the temperature and length differences (Fig. 6.4).

Thermocouples have relatively small outputs ($\sim 40\,\mu$V/°C for copper constantan), but this is not a serious disadvantage now that stable dc amplifiers are available. Absolute temperature measurement is less convenient with thermocouples because of the need for a stable temperature reference. Copper leads can be used for measurements at a distance from the amplifier, but care must be taken to keep the lead junctions at the same temperature (see Fig. 6.5).

Thermistors have high (negative) temperature coefficients of resistance, about 10 times those of platinum-resistance thermometers, but their thermal dissipation rates make self-heating a problem, tending to reduce the available sensitivity drastically. Nonlinearity in output and poor long-term stability are problems common to thermistor probes.

The ideal choice for a temperature profile system is the quartz thermometer. Its output is a beat frequency that varies linearly with temperature, and its basic

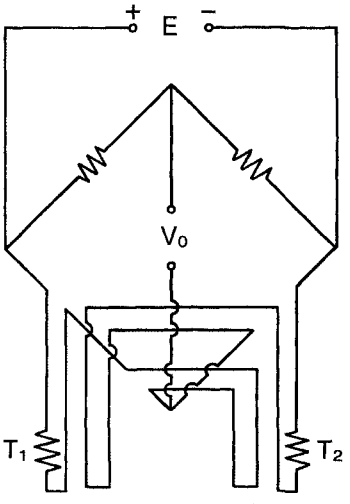

FIG. 6.4 Typical bridge circuit with lead compensation for a platinum-wire thermometer.

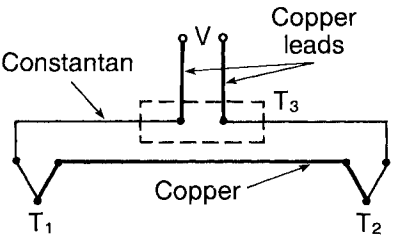

FIG. 6.5 Thermocouple configuration with external junctions kept at the same temperature.

accuracy (0.001°C) is degraded only by the errors (±0.05°C) introduced by the radiation shield and the aspirator. The main drawback is its cost, but the benefits of trouble-free performance may make it worth the cost for many applications.

Several types of aspirated radiation shields are available. They all perform reasonably well except at very low sun angles, where some designs do not provide adequate shielding. Wind-aspirated shields mounted on vanes have, in general, not proved satisfactory.

6.1.3 *Mean humidity sensors*

Humidity is among the more difficult variables to measure in the boundary layer. Many different definitions are used to specify the water vapor content of air: vapor pressure (in mb), absolute humidity (mass per unit volume), specific humidity (mass of water per mass of moist air), and relative humidity (mass of water in air per mass of water in saturated air at the same temperature and pressure).

Dewpoint (or frostpoint) hygrometers provide absolute measurement of humidity, whereas psychrometers that measure wet-bulb depression yield specific humidity through the psychrometric equation. Hygroscopic devices that respond to changes in relative humidity are simpler to use but usually depend on curves provided by the manufacturer for calibration.

For applications in which accuracy and long-term stability are of critical importance, the dewpoint hygrometer would be the most logical choice. In this device, a mirrored surface is maintained thermoelectrically at the temperature at which the moisture in the air begins to condense or freeze on it (Fig. 6.6). The temperature of the mirror is sensed by a platinum resistance thermometer, thermocouple, or thermistor. The device is generally housed in an aspirated shield. The sensor requires periodic cleaning of the mirror surface and checks of the calibration adjustments; with reasonable maintenance, absolute accuracies of ±0.5°C are attainable.

The psychrometric technique, used widely in field experiments, is inexpensive (compared with the cost of dewpoint devices), simple in concept, and relatively easy to maintain. It consists of two identical ventilated temperature sensors,

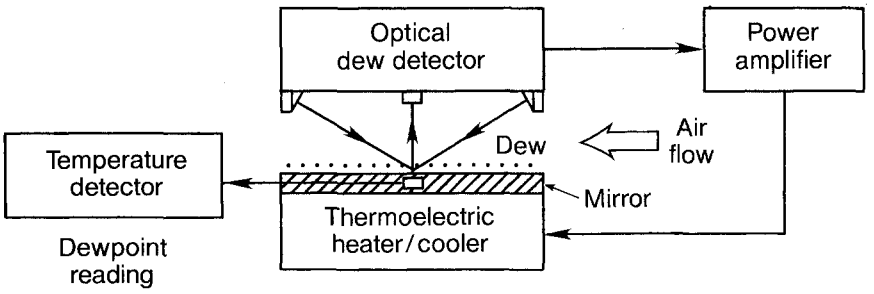

FIG. 6.6 Optical dewpoint hygrometer.

one of which is covered with a wick saturated with distilled water. Great care is needed in its design to ensure proper shielding from solar radiation, adequate ventilation, and wetting of the wick. The accuracy of this system is low at low humidities and temperatures, but is usually assessed in terms of the reading at 100% relative humidity. Accuracies of 0.5–1.0°C equivalent dewpoint temperatures can be maintained over a 20% to 80% relative humidity and a 0–25°C temperature range. The errors increase sharply below freezing because it is difficult to form and maintain an ice bulb on the wet thermometer. An example of an aspirated, radiation-shielded psychrometer of a type successfully used at Commonwealth Scientific and Industrial Research Organization (CSIRO) is shown in Fig. 6.7. This radiation shield is not affected by rays from low sun angles.

The hygroscopic sensors are also relatively inexpensive and easy to use. The Väisälä humicap is one of the more widely used sensors of this type. It responds to humidity with a capacitance change. The sensor provides a voltage directly proportional to relative humidity. Among its common failings are hysteresis effects, susceptibility to contamination, and loss of accuracy at high relative humidities. Because the humicap senses relative humidity, the air temperature must also be measured before absolute humidity can be obtained. Zero drifts caused by any of the effects mentioned above mean that sensors must be interchanged regularly if they are used for profile measurements. In practice, humicaps are often used not as in situ sensors but in the bench-mounted mode, held at a known reference temperature, taking measurements of air drawn along tubes from the sampling points. In this arrangement, it may be necessary to heat the tubes to avoid condensation when relative humidities are high.

6.1.4 *Trace gas sensors*

The most important trace gases in the atmosphere, from the biological point of view, are water vapor and CO_2. Mean concentrations of both these gases can be measured with great accuracy by infrared gas analyzers (IRGA). Standard IRGAs are bench-mounted instruments that must be shielded from vibrations and placed

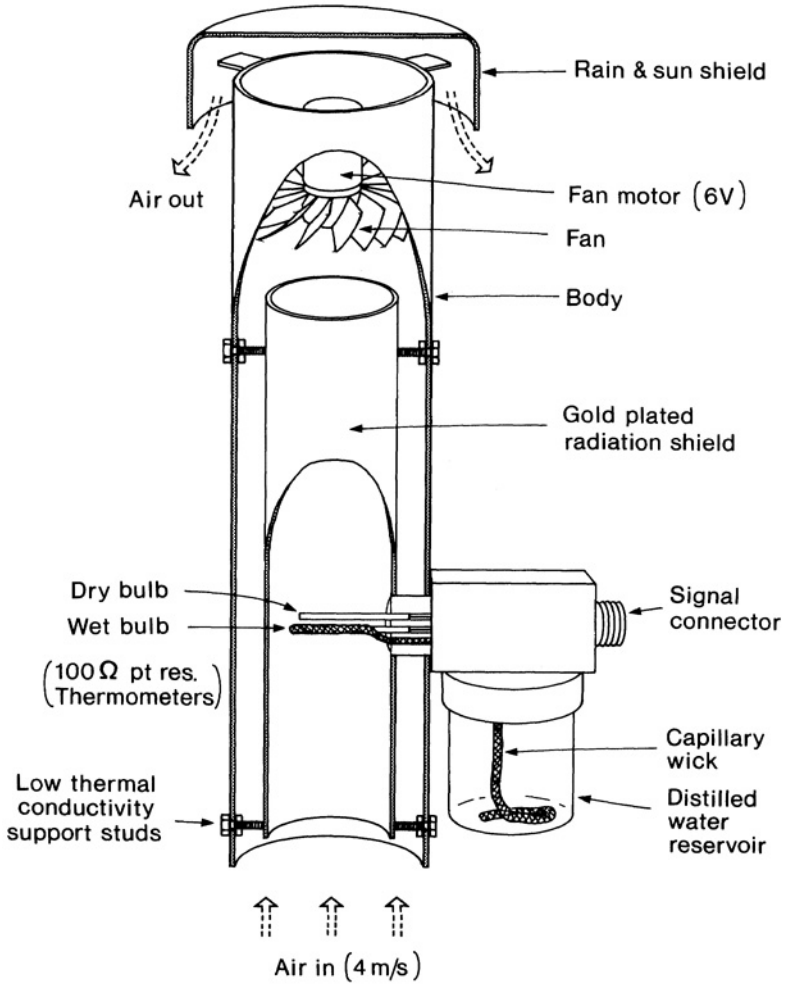

Fig. 6.7 CSIRO aspirated radiation-shielded psychrometer.

in a relatively stable temperature environment. They operate by comparing the absorption of infrared radiation in a sample of air drawn from the measurement point with that in a reference sample of accurately known concentration (Szeicz, 1975). For measuring CO_2, a reference sample containing a known amount of CO_2 would be used, but to measure water vapor a reference sample containing NH_3 or ethane, gases that absorb infrared in the same bands that absorb water vapor, would be used.

Other gases that can be conveniently measured with IRGAs are N_2O, CO, SO_2 (although not in trace amounts), and CH_4. The IRGA is a slow-response device requiring a minute or so to come to equilibrium with the sample. It can,

however, be used in a continuous flow mode so that concentration variations are obtainable, albeit with this rather long time constant. Further detailed discussions of techniques used for trace gas measurements will be found in Andreae and Schimel (1989).

6.2 In situ sensors for turbulence measurements

6.2.1 *Velocity fluctuation sensors*

The hot-wire anemometer is the sensor traditionally used in turbulence work. It is best suited for laboratory and wind tunnel studies in which the dimensions of the sensor have to be small (on the order of millimeters) and the frequency response high (on the order of 10 kHz). For boundary layer flux measurements, the excellent frequency response of the hot-wire anemometer does not make up for its three major drawbacks: susceptibility to calibration shifts from atmospheric contamination, fragility, and narrow wind acceptance angle. The spatial scales of interest in the boundary layer range from 1 m to 10 km, and continuous measurements are sometimes needed for periods ranging from days to weeks. In such applications, the sonic anemometer is the preferred instrument; it has none of the response problems associated with rotating-type anemometers. The high cost of sonic anemometers, however, has led many researchers to look for simpler and less expensive options such as dynamic anemometers. Dynamic anemometers measure wind velocity by sensing either the pressure or the drag force on an object placed in the flow. They include thrust anemometers, anemoclinometers, and vortex anemometers. They respond to fluctuations in the wind more slowly than sonic anemometers but more quickly than the rotating types. Most of these devices are custom-made at various laboratories and are not available commercially. The types of sensors currently used for measuring wind fluctuations in most low-budget applications are configurations of lightweight propeller anemometers and bivanes offered by manufacturers of meteorological instruments.

Sonic anemometers measure wind velocity by sensing the effect of the wind on transit times of acoustic pulses traveling in opposite directions across a known path. The main limitation to their frequency response is imposed by line averaging along the path, which we will discuss later in the context of array geometries. Sonic anemometers can be of either the pulse type or the continuous-wave type. The former measures transit time differences directly to compute the velocity component along the path, whereas the latter measures phase differences that can be converted to time differences. Both measurements relate directly to wind velocity (see Appendix 6.1). The velocity component, V_d, along path length d, can be expressed as

$$V_d = \frac{c^2}{2d}(t_2 - t_1), \tag{6.2}$$

where c is the velocity of sound in air and t_1 and t_2 are the transit times for sound pulses traveling downwind and upwind along parallel paths. If c and d are known, V_d reduces to the measurement of $(t_2 - t_1)$, a relatively simple time interval measurement. For most applications, the velocity of sound can be approximated by

$$c^2 = 403\,T(1 + 0.32e/p), \tag{6.3}$$

where T is the absolute temperature, e is the vapor pressure of water, and p is the atmospheric pressure, all expressed in SI units. The contribution of e/p is small and usually neglected. Thus c^2 in (6.2) can be replaced by $403\overline{T}$, where $\overline{T}$ is the average temperature for the observing period. In the earlier sonic anemometers, $(t_2 - t_1)$ was measured electronically and adjustments in the calibration made during data analysis for variations in the mean temperature. Two separate paths were then used for simultaneous transmission of pulses in opposite directions.

The advent of integrated circuits and microprocessors opened the way for a more direct approach to measuring velocity through the relationship (Appendix 6.1):

$$V_d = \frac{d}{2}\left(\frac{1}{t_1} - \frac{1}{t_2}\right). \tag{6.4}$$

Newer sonic anemometers of the type described by Coppin and Taylor (1983), Hanafusa et al. (1980), and Kaimal et al. (1990), among others, exploit this fact; two of the above systems even extract temperature from the reciprocals of t_1 and t_2 (Appendix 6.1), as we shall see in the section to follow. All three use a single path to transmit sound pulses back and forth and measure t_1 and t_2 separately, thus reducing the number of transducers needed in the probes. (The transducers at the end of each path serve alternately as transmitters and receivers.) The first two, produced commercially by Kaijo Denki, Inc. (Japan) and Dobbie Instruments (Australia), have nonorthogonal path configurations (Figs. 6.8 and 6.9). The third, produced by Applied Technologies Inc. (US), offers an orthogonal path configuration (Fig. 6.10). They all have their paths arranged to measure one vertical and two horizontal wind components,[1] but the different arrangements of the paths reflect different needs and operating philosophies. (Kaijo Denki and Applied Technologies offer other probe configurations as well.)

The probes in Figs. 6.8 and 6.9, with their 120° separation between the horizontal axes, are designed to face the wind for best results. For winds within

[1] A different nonorthogonal configuration, using three intersecting paths tilted 30° from the vertical in an equilateral arrangement, has been described by Zhang et al. (1986). Commercial versions using that concept are available from Kaijo Denki, Inc., and Solent Instruments, Ltd. (UK).

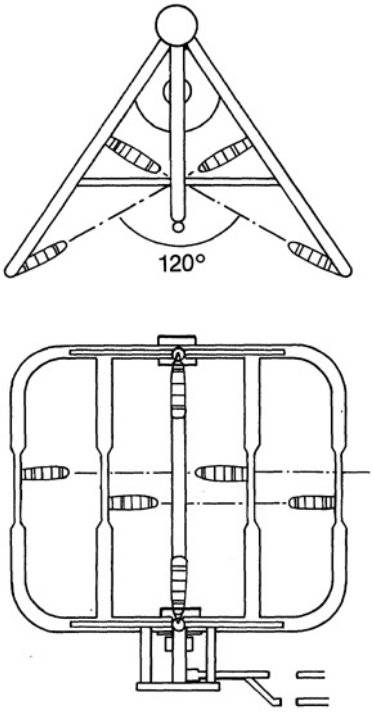

Fig. 6.8 Kaijo Denki single-path ($d = 0.2$ m) nonorthogonal sonic anemometer-thermometer probe.

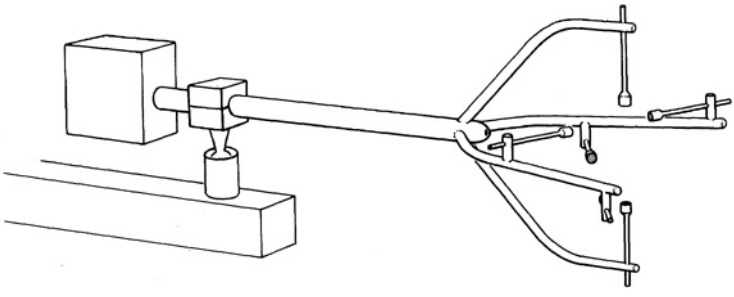

Fig. 6.9 CSIRO/Dobbie single-path ($d = 0.1$ m) nonorthogonal sonic anemometer probe.

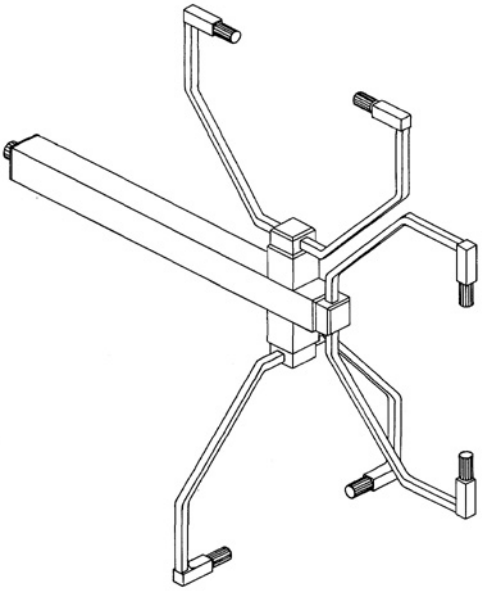

Fig. 6.10 Applied Technologies single-path ($d = 0.15$ m) orthogonal sonic anemometer-thermometer probe.

an azimuth range of $\pm 30°$ from the probe's central axis (Grant and Watkins, 1989), the horizontal wind readings require no correction for shadowing by the structural supports or transducers at the upwind end of their paths. In order to benefit from this design, it is essential that the probe be reoriented periodically into the mean wind direction. The transformation equations for this array are given in Appendix 6.2. The CSIRO/Dobbie probe,[2] with its short path and vertically offset horizontal axes, operates on the same principle but offers a more compact measuring volume ($\sim$12-cm-diameter sphere) for use in plant canopies, close to branches and leaves and to within 1 m of the ground. Here, we accept a higher degree of flow distortion and transducer shadowing (Wyngaard and Zhang, 1985) as the price for compactness in the sampling volume and consequent improvement in frequency response.

The probe in Fig. 6.10, on the other hand, is designed for fixed operation at the end of a boom and aims to correct, in real time under microprocessor control, any deviations from cosine response due to upwind obstructions to the flow. By separating vertically the two horizontal paths, the error reduces to only the deficit due to shadowing by the transducers at the ends of horizontal paths. The form of the velocity deficit varies with the probe and the transducer shape (Wyngaard and Zhang, 1985); it is maximum for winds blowing along the axis

[2] Parallel versions of the original CSIRO and Dobbie versions are in use.

and drops off gradually as the wind deviates from that direction. Response curves for Applied Technologies' 1-cm-diameter transducer are presented in Appendix 6.3, plotted as a function of path length-to-transducer diameter ratio. The 37-cm vertical separation in the horizontal paths has been shown to have negligible effect on the observed mean and turbulence statistics at 10 m and 22 m over flat ground (Kaimal et al., 1990). The probe is not recommended for use below 4 m where the vertical gradients of wind speed are typically the largest and the eddy scales of interest too small to be resolved accurately by this probe.

As pointed out earlier, the main limitation to the frequency response of the sonic anemometer is the one imposed by line averaging along the acoustic paths. Spatial separation between the paths also introduces distortions at the high-frequency end; its effect is mostly felt in the transformed horizontal wind components u and v, which are derived primarily from measurements along spatially separated horizontal paths. A rough rule of thumb for calculating the onset of spectral distortion attributable to path length d, or separation distance s, is $\kappa_1 d$ or $(\kappa_1 s) = 1$, where κ_1 is the streamwise wavenumber ($\simeq 2\pi f/\overline{u}$), as defined in Chapter 1. The larger of the two effects determines the onset frequency, which we will define here as the 98% power cutoff.

The exact form for the spectral response in the wind components therefore depends on the length of the paths and orientation with respect to the mean wind direction. Kaimal et al. (1968) had shown that the line-averaging effect for the w component (from a single vertical path) approximates that of a single-pole, low-pass filter with half-power point at λ (or $\overline{u}/f$) = d, as shown in Fig. 6.11. In the nonorthogonal array of Fig. 6.8, the power spectral responses for u and v differ from that of w because of the spatial separation ($s \approx 0.6d$) between the horizontal paths. For all three, however, the roll-off starts at $\lambda \approx 2\pi d$ (or 1.25 m for d = 20 cm).

In the case of the orthogonal probe in Fig. 6.10, the 37-cm vertical separation between the horizontal axes determines the useful wavelength range for u and v measurements; it will be $\lambda > 2\pi \times 37$ cm, compared with $\lambda > 2\pi \times 15$ cm for w. For measurements above 4 m height over flat terrain this will not seriously degrade the estimations of $\overline{u'w'}$ and $\overline{w'\theta'}$ since the bandwidth requirements for the two fluxes also differ by a factor of 2.5, as seen in Fig. 2.18. Over complicated topography and in canopies, however, this benefit may not be realized because the w path may not be normal to the mean wind vector. In that case, it is wise to assume a sampling diameter that includes not only the sonic paths but also any scalar sensor contributing measurements for flux calculations.

It is instructive to compare the dynamic responses of the bivanes (vanes that can rotate vertically as well as horizontally) and propellers used in atmospheric work with those of the sonic anemometer. Manufacturers' specifications list delay distances for bivanes (50% recovery) and distance constants for propellers (63% of step change) as being close to 1 m. These distances, however, translate to much

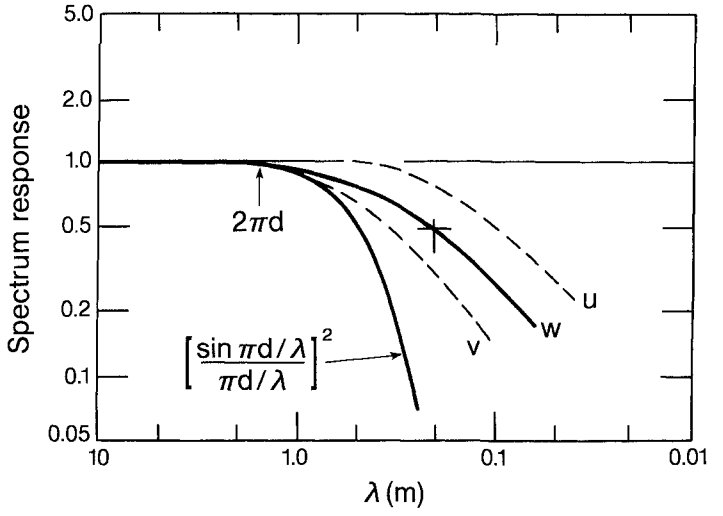

FIG. 6.11 Power spectral transfer functions for u, v, and w in a three-axis sonic anemometer with $d = 0.2$ m and 120° separation between the horizontal axes for wind blowing along the probe's central axis. The $(\sin^2 x)/x^2$ function representing simple line averaging along the direction of the flow is shown for comparison (after Kaimal et al., 1968).

longer cutoff wavelengths if we define the response in terms of departures from the ideal spectral response (Finkelstein et al., 1986). Figure 6.12 shows response functions for the vertical wind component w measured by R. M. Young's bivane system and the Gill propeller anemometer. These functions were derived from comparison tests with a sonic anemometer at 10 m height. Defining λ_c, the cutoff

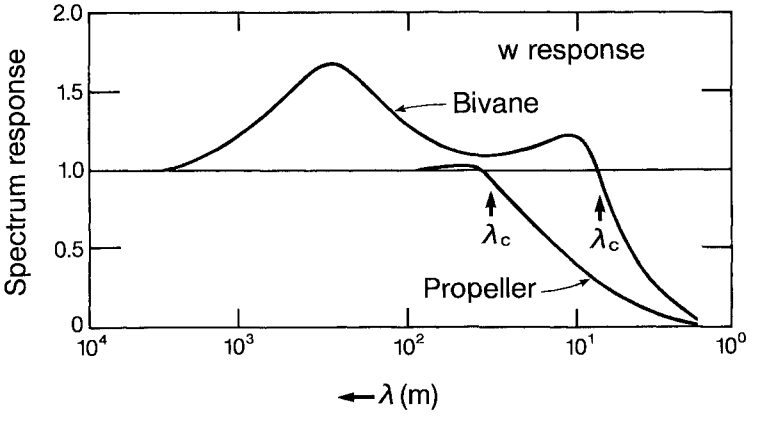

FIG. 6.12 Power spectral transfer functions for the w component measured by a propeller bivane and a single vertical propeller anemometer (after Finkelstein et al., 1986).

wavelength, as the point where the power spectrum drops to 98% of its true value, we find λ_c to be 32 m for the vertical propeller and 7 m for the propeller-bivane combination.

The bivane's response to w appears to be superior to that of the propeller for $\lambda < 32$ m, but the amplification at the middle frequencies raises concern as to its effect on flux calculations. To a moderate degree, the enhancement in the variance is beneficial because it compensates for the high-frequency cutoff; vertical velocity variances from the bivane compare very closely with sonic anemometer values. The propeller w variances, on the other hand, are severely underestimated: 25% lower under daytime conditions and up to 50% lower under nighttime conditions, at 10 m height.

The large λ_c value for the w propeller is not surprising when we consider the off-axis degradation in response and the relationships that exist between distance constant l, half-power wavelength λ_0, and λ_c. The distance constant for the Gill propeller increases from 1 to 2 m as the flow deviates from axial to 80° off axis. In principle, the distance constant approaches infinity at 90° off axis.

For a linear first-order system, the power transfer function can be written as

$$[H(\lambda)]^2 = \frac{1}{1 + (2\pi l/\lambda)^2}. \tag{6.5}$$

At the half-power point we have

$$\lambda_0 = 2\pi l, \tag{6.6}$$

and λ_c, defined here as the 98% power point, becomes

$$\lambda_c = 2\pi\lambda_0 \simeq 40l. \tag{6.7}$$

With $l = 2$ m (for the w measurement), λ_c would be 80 m for a linear first-order system. Fortunately, the propeller's response is better by a factor of 2.5 (Fig. 6.13), which brings the actual value of λ_c down to 32 m as observed.

6.2.2 *Temperature fluctuation sensors*

Fine-wire platinum-resistance thermometers, thermocouples, thermistors, and sonic thermometers have all been used for temperature fluctuation measurements. Thermistor and thermocouple sensing elements cannot be made as small as platinum wire probes, so they tend to be less responsive and not as well suited for flux measurements near the ground. All three types are normally exposed to free air without the benefit of protection from radiation shields. They are, therefore, vul-

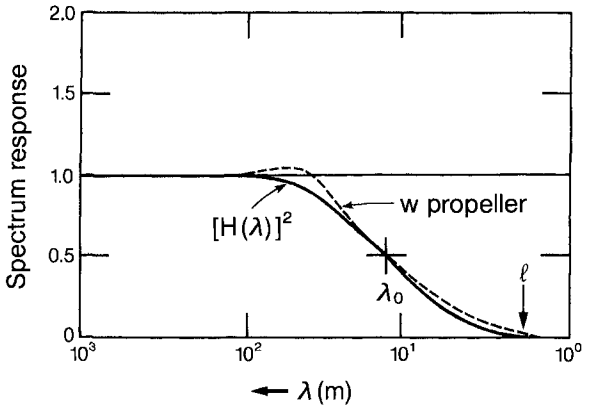

FIG. 6.13 Response of a single vertical propeller compared with first-order linear response showing the disparity between half-power wavelength λ_0 and distance constant l (after Finkelstein et al., 1986).

nerable to damage from winds, rain, snow, and flying debris. The chances of damage can be reduced significantly if the element is properly supported. Such supports increase the time constant of the sensor. The 12.5-μm platinum wire in the fast-response probe (also marketed by Atmospheric Instrumentation Research) used at the Boulder Atmospheric Observatory (BAO) (Kaimal and Gaynor, 1983) is wound around a small helical bobbin on threads strung across the windings of the helix. The spectral response of the wire is degraded by conduction through the support, but only at frequencies above 5 Hz. With this support, the sensing element can survive for weeks and even months without breaking. Freezing rain, wet snow, and very high winds are the events that usually break the wire. It should be pointed out that platinum wires should not be left exposed to the elements for too long. Contamination of the wire has a direct effect on its time constant. A convenient scheme for calibrating the platinum wire probe in the field is illustrated in Fig. 6.14. Switching in a fixed resistance changes the current flowing through the wire by an amount corresponding to a known temperature change (5°C). The amplifier gain is adjusted to set the corresponding step change in the output voltage of the temperature circuit to 5 V to match the input calibration requirement in the data acquisition system. A small flask is slipped over the platinum wire probe to suppress the fluctuations in the signal while this calibration is in progress. This procedure compensates for probe-to-probe variations in resistance and even changes due to aging.

The sonic thermometers incorporated in the Kaijo Denki and Applied Technologies sonic anemometers have the requisite frequency response for boundary layer flux measurements. Temperature is sensed along the same path as w, so its spatial averaging characteristic is compatible with that of w. The sonic temperature, which is proportional to $[(1/t_1) + (1/t_2)]^2$, is, however, contaminated by

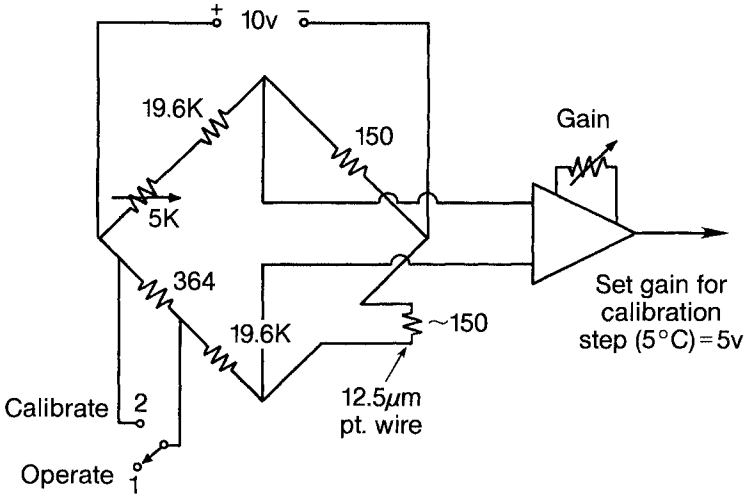

FIG. 6.14 Switching arrangement for field calibration of a fast-response platinum wire thermometer.

residual sensitivities to humidity and to the wind component normal to the path. These errors are negligible under daytime unstable conditions when temperature fluctuations are large. The wind contamination, in particular, however, can be significant under near-neutral and stable conditions (Kaimal, 1969). The nature of the cross-wind contamination on the evaluated heat flux is such that it introduces a bias in the estimation of the time the atmosphere passes through neutral stability, shifting it slightly into the stable regime. We show in Appendix 6.1 how the crosswind velocity (V_n) modifies the sonic thermometer equation:

$$\frac{1}{t_1} + \frac{1}{t_2} = \frac{2}{d}(c^2 - V_n^2)^{1/2}. \tag{6.8}$$

Substituting for c^2 from (6.3) we have, for the temperature measured along the vertical path,

$$T(1 + 0.32e/p) = \frac{d^2}{1612}\left(\frac{1}{t_1} + \frac{1}{t_2}\right)^2 + \frac{1}{403}\left(V_X^2 + V_Y^2\right), \tag{6.9}$$

where V_X and V_Y are the wind components along the orthogonal horizontal axes of the anemometer and all variables are expressed in SI units. In the Applied Technologies sonic thermometer (Fig. 6.9), V_X and V_Y, compensated for transducer shadowing, are used to correct, in real time, each temperature reading as it is processed for transfer to its output registers.

The humidity term and its effect on calculated variances and fluxes can be ignored, as is often done, or compensated for in the data analysis if concurrent measurements of humidity fluctuations are available. Kaimal and Gaynor (1991) argue that the sonic-derived temperature on the left in (6.9) should be treated as the true virtual temperature T_v, which it approximates very closely since

$$T_v = T(1 + 0.38e/p), \tag{6.10}$$

and could be used directly in its place in applications where the contribution to buoyancy from moisture should be included. A case in point is the Obukhov length L, where the temperature flux term should, in the presence of moisture, be $\overline{w'T_v'}$ (for most applications we assume $\theta_v' = T_v'$). The V_n^2 corrected temperature from the sonic thermometer approximates T_v to within 0.01°C, well within the bounds of experimental uncertainty.

6.3.2 *Humidity fluctuation sensors*

Three different techniques are currently used for measuring humidity fluctuations. They involve the absorption of ultraviolet radiation by water vapor (Lyman-alpha and krypton hygrometer), the absorption of infrared radiation by water vapor (infrared hygrometer), and the dependence of microwave refractivity on humidity (microwave refractometer).

The simplest of the three devices is the ultraviolet hygrometer. The Lyman-alpha version requires a source (excited hydrogen), a nitric oxide detector, and a space between the two where the absorption takes place (see Fig. 6.15). Magnesium fluoride windows are needed on the source and detector tubes since most other materials are opaque to ultraviolet radiation. The cutoff frequencies of the nitric oxide detector and the magnesium fluoride windows neatly bracket the Lyman-alpha emission line of atomic hydrogen (121.56 nm). The other emission lines in the hydrogen glow discharge produced by the source are thus filtered out.

The very strong absorption of this emission line by water vapor makes measurement possible over short path lengths ($\sim$1 cm). (By comparison, absorption by ozone and oxygen, the only other absorbers in the atmosphere, can be neglected in the boundary layer.) The dimensions of the sensor are small enough (15 cm long $\times$ 2 cm diameter) to permit installation close to a sonic anemometer. For uniform exposure in the azimuth, the sensor is mounted with its path oriented vertically. Two sources of drift in the calibration should be noted: aging of the Lyman-alpha source and window degradation from reaction of atmospheric constituents with the window material. The effect of aging is retarded to some extent by using higher hydrogen pressures and sealing uranium hydroxide in the source body. The window degradation is reversible, since it occurs on the outer surface; washing with alcohol and rubbing with a fine abrasive restores its transmission

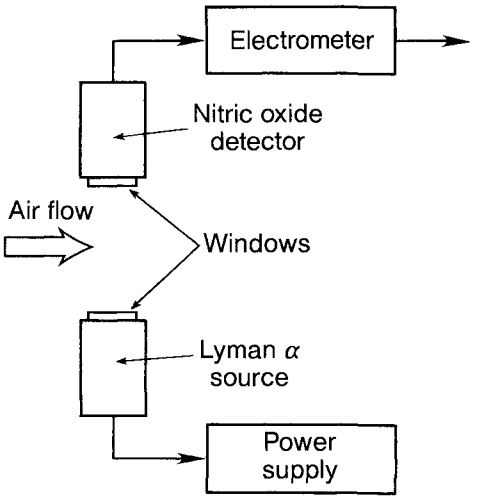

FIG. 6.15 Lyman-alpha hygrometer (after Buck, 1976).

properties. Nevertheless, for maximum accuracy, this device should be operated in conjunction with a dewpoint hygrometer, so its calibration can be continuously updated by comparing changes in its mean readings with those derived from the slower, more accurate, dewpoint measurements.

In the krypton hygrometer, the ultraviolet source is a krypton glow tube. This produces ultraviolet emission at 123.58 and 116.47 nm, rather than the 121.56 nm of the hydrogen line. In all other respects they operate the same way. The advantage of the krypton device is the long-term stability of the source in comparison with the degradation over time of the hydrogen source. The disadvantage is the greater absorption of the krypton lines by oxygen and ozone. In practice, this does not pose a severe problem, and reliable commercial krypton hygrometers are now available.

The infrared hygrometer detects humidity through differential measurement of infrared transmittance at two adjacent wavelengths, one located in a region of high water vapor absorption and the other where the absorption is negligible. The transmitting path is typically 0.2–1.0 m long, and the beams are usually modulated by a mechanical chopper to permit high-gain amplification of the detected signal. Optical components such as narrow-band filters and beamsplitters add to the complexity of this device.[3] At humidities approaching saturation, the calibration is undependable because of scattering from water adsorbed and absorbed by particles in the air.

[3]Recently, Y. Mitsuta and colleagues at the Kyoto University Disaster Prevention Research Institute have claimed success with a simpler single wavelength infrared system in which the filament temperature at the source is varied sinusoidally for stability in the humidity measurements (personal communication).

The microwave refractometer measures the refractive index of air in a cavity and depends on the relationship between refractivity, specific humidity, temperature, and pressure to derive humidity. Strictly speaking, simultaneous data on temperature and pressure fluctuations in the cavity are needed to remove their influence on the refractive index; in practice, pressure fluctuations are ignored since they are usually small (<1 mb) compared with the absolute pressure. The temperature measurement is made as close to the cavity as possible. The sensing element in the microwave refractometer is a resonating cavity with ventilating ports. The cavity dimensions are small, but the spatial resolution of the sensor is more a function of its flushing efficiency than of its actual size. For a 5-cm cavity, in moderately light winds, spectral attenuation starts at a wavelength of 1.5 m. In an experiment comparing various humidity sensors, Priestley and Hill (1985) found the refractometer response falling off rapidly at 2 Hz with wind speeds at 3–4 m s^{-1}. The Lyman-alpha hygrometer's response under the same conditions extends another decade, to 20 Hz.

6.2.4 *Trace gas fluctuation sensors*

Infrared absorption by CO_2 occurs at a different wavelength than water vapor. In recent years successful rapid-response open-path devices working on the same principle as infrared hygrometers have become available. The commercial versions measure both CO_2 and water vapor simultaneously. Recently the same technique has been extended to CH_4 at yet another infrared wavelength. Absorption of gases such as CO_2 and SO_2 at very low concentration is strongly modulated by density changes caused by temperature and water vapor fluctuations. The required corrections for measured eddy fluxes of the trace gases amount to 100% or more over freely transpiring vegetation (Webb et al., 1980), making such measurements over water problematic at best.

6.2.5 *Static pressure fluctuation sensors*

The most difficult dynamic variable to measure in a strongly turbulent flow is the static pressure fluctuation p' because any probe introduced into the airstream causes dynamic pressure fluctuations $p'_d = \rho(u'_p)^2/2$, where u'_p is the local velocity variation caused by the probe. p'_d is typically an order of magnitude larger than the desired static pressure fluctuation p'. If the probe can be aligned to within a few degrees of the wind vector, then sampling ports can be arranged so that contributions to p'_d from ports at different points on the probe cancel out, leaving the required signal p'. In turbulent flows where the instantaneous wind vector varies rapidly about the probe axis, an optimum configuration for the ports is much more difficult to achieve.

One successful probe design for surface layer studies is described by Elliot (1972). His spoon-like probe is relatively insensitive to wind angles of attack

within $\pm 135°$ in the azimuth and $\pm 15°$ in elevation. This restriction limits its use to measurements in relatively low-intensity turbulence. A new omnidirectional probe claiming acceptance angles of $\pm 30°$ in elevation has been described by Nishiyama and Bedard (1991). Their probe consists of a series of outer and inner ports arranged in rings around a vertical tube fitted with four discs as shown in Fig. 6.16. The width and placement of the discs provide cancellation of dynamic pressure changes at the inner ports over the $\pm 30°$ range of elevation angles. The probe can operate in adverse environments. This probe has been deployed in field experiments and awaits confirmation of its usefulness for measuring p' in turbulent kinetic energy budget studies.

6.3 Sensors for surface measurements

Heading this list are sensing techniques that have been used for decades to measure the parameters needed to calculate energy balance at the earth's surface. The energy balance at the surface can be written, in its simplest form, as

$$R_n - G_s = H + \lambda_e E,$$

where R_n is the net radiation flux density at the surface, G_s is the flux of heat into the soil, H is the sensible and $\lambda_e E$ the latent heat flux from the surface as defined in Chapter 3. R_n and G_s are routinely measured with net radiometers and soil heat flux plates, respectively, whereas $\lambda_e E$ can be measured directly with a lysimeter. We also discuss the use of drag plates to measure the momentum flux at the surface directly. Its disuse in recent years notwithstanding, the drag plate remains the only sensor capable of measuring unequivocally the momentum flux at the surface, invaluable in situations in which the constant flux assumption cannot be invoked. Also included is radiometric sensing of surface temperature because of its increasing use in boundary layer studies.

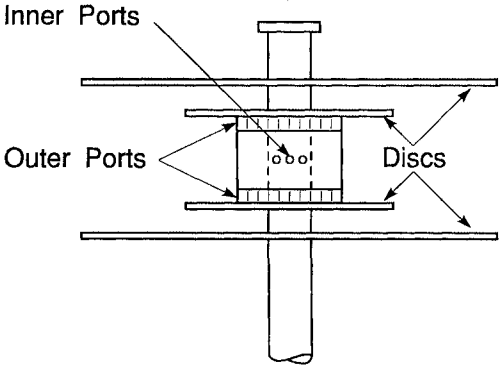

Fig. 6.16 Omnidirectional pressure fluctuation sensor (after Nishiyama and Bedard, 1991).

6.3.1 *Net radiometers*

Net radiometers measure the difference between total (all wavelength) incoming and outgoing radiation. The standard version of the instrument consists of two small ($\sim$ 20 mm square) black surfaces facing up and down, separated by an insulator and protected from the wind by polyethylene hemispherical domes, as shown in Fig. 6.17. The temperature difference between the upper and lower surfaces drives a thermopile so that the unamplified signal from the radiometer is typically a few millivolts. The whole assembly is mounted at the end of a tube 1 m long. In radiometers with thin polyethylene domes (Funk type), the space enclosed by the domes is ventilated with a supply of dry inert gas that also keeps them inflated; those with rigid polyethylene domes (Fritschen type) are usually not ventilated, but an external tube of desiccant is plumbed to the spherical space around the thermopile to prevent condensation.

Because R_n is usually the small difference between two large numbers, great care must be taken with calibration and installation of the instrument. The radiometer must be carefully leveled and the downward-looking hemisphere should "see" a representative section of the ground. Over short vegetation or bare soil, the radiometer is mounted about 2 m above the surface on its own mast, but over taller plants, as in forest canopies, it may be necessary to use a tall instrument tower. In such cases the radiometer should be mounted at the end of a long boom to remove as much of the tower as possible from the field of view of the radiometer. Ingenious arrangements are necessary to level an instrument that may be 4–5 m out from the tower. More discussion of net radiometers can be found in Szeicz (1975).

6.3.2 *Soil heat flux plates*

The sensible heat flux across the soil surface is commonly measured directly with soil heat flux plates. These are available commercially and consist of metal plates ($\sim$10 cm^2 in area) separated by a material of known conductivity. The temperature

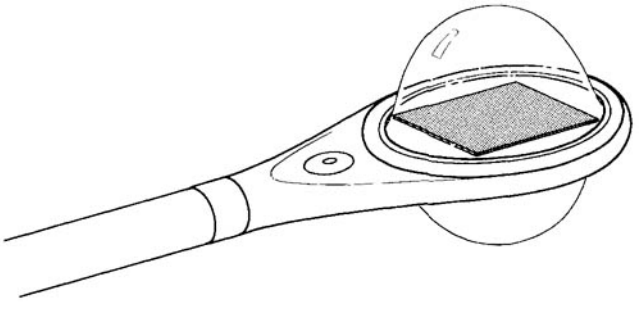

Fig. 6.17 Funk net radiometer.

differences between the plates drive a thermopile that provides the sensor output. Three or four such plates are usually connected electrically and distributed a few millimeters below the soil surface at representative locations. Errors arise through sampling problems if the surface is heterogeneous. More serious errors occur in a drying soil where the site of soil evaporation has moved below the surface and a significant fraction (~50%, at times) of energy flux to the ground is through diffusion of water vapor in the upper soil layers. These problems are discussed in detail by deVries and Philip (1986).

6.3.3 *Lysimeters*

In the weighing lysimeter, a block of soil large enough to be a representative sample of the surface and deep enough to contain the roots of any plants present is isolated from the surrounding soil in a watertight container mounted on a sensitive, continuously recording balance. The balance must be capable of resolving a few tens of grams, whereas the block itself may weigh several tons. Both the water running off at the surface during rain and the water percolating through the soil monolith past the roots are collected and recorded, while the time record of the change in the weight of the lysimeter itself gives the evaporation rate. A small correction may have to be made for plant growth over the long term. The accuracy obtainable from a lysimeter depends ultimately on the representativeness of the sample. This may be as small as 1 m^2 in an area over short grass or bare soil, whereas forest lysimeters covering areas more than 10 m^2 and containing mature trees have also been operated successfully. For the large lysimeters, excavating the soil monoliths in situ with minimum disturbance to the sample is a major undertaking. For more information see Dunin et al. (1991).

6.3.4 *Drag plates*

The same principle embodied in the lysimeter is used here to measure the flux of momentum to the surface, $\tau_0 = \rho u_*^2$. The drag plate consists of a representative sample of the ground surface mounted on a sensitive balance designed to measure the tangential force on the surface. The entire mechanism is buried beneath the ground so that no surface discontinuity or disturbance is apparent to the observer above. Typical drag plate configurations have circular platforms 1–2 m in diameter, deep enough (~10 cm) to hold sufficient soil to keep short vegetation alive for the duration of an experiment. The weight of the plate imposes severe demands on the mechanical structure supporting it. Also, the gap around the rim of the sample has to be very small (a few millimeters) to keep spurious aerodynamic pressure forces from swamping the small tangential forces due to τ_0, requiring essentially zero deflection under load. All these requirements lead to a heavy, high-precision device of the type described by Lynch and Bradley (1972). The drag plate approach

is best suited for use over flat homogeneous surfaces with adequate fetch, bare or covered with short vegetation such as mowed grass or wheat stubble.

6.3.5 *Radiometric thermometers*

It is sometimes necessary to have a measure of surface temperature. Over bare soil, the surface temperature may be measured directly with an in situ thermometer; but over vegetated surfaces, infrared thermometers mounted on towers, aircraft, or satellites offer a means to measure that quantity remotely without the sampling limitations inherent in the in situ approach. Errors arise from many sources such as the dependence of soil surface emissivity on water content and surface texture, the "cool-skin" effect on open water bodies, and the difference between bulk aerodynamic temperature and radiometric temperature in plant canopies. A vast literature has recently bloomed on this subject.

6.4 Measuring from towers and masts

Towers, masts, booms, and mounts used for supporting a sensor can interfere with the flow, thus introducing errors in the measured gradients and fluxes. It is possible to reduce these errors to acceptable levels if care is exercised in the design of the supporting structure and placement of the sensors. There is considerable discussion on this subject in the literature. No simple solutions or relationships for flow distortion have emerged because the geometries of the obstacles discussed vary so greatly (Wucknitz, 1980). Upwind of the tower we need to consider two distinct regions of the disturbed flow: one close to the obstacle, at distances smaller than the diameter of the obstacle, where the flow is complicated and difficult to describe theoretically; the other at distances greater than the diameter, where potential flow can be assumed in order to calculate flow distortion.

The first region is one the experimenter would do well to avoid. For a tower with structural members that are small and widely separated (ratio of obstructed-to-unobstructed area < 0.1), we might consider installing sensors at upwind distances smaller than the outside dimensions of the tower. Most towers have structural member densities between 0.2 and 0.3. In that case, the sensors should be mounted no closer than 1.5 times the largest lateral dimension of the tower. (Up to 4 times the tower width is possible with certain portable and guyed TV-antenna-type towers that have lateral dimensions on the order of 0.3 m but are capable of reaching up to 60 m.) In applications where only one level of observation is needed (say at 10 m), the anemometer should be mounted on top of the tower (or mast) to avoid direct tower shadowing. To reach the region where potential flow can be assumed, the sensor has to be at least three lateral dimensions above the top of the tower and supported by a thinner mast.

Another region of the flow to be avoided is the downwind side of the tower. At the very least, readings from this region should be treated with caution. Here,

the flow is strongly influenced by the wake structure. Even on towers with low structural member densities, the combined effect of wakes from the separate members can be greater than for a solid tower offering the same obstruction area to the flow. The wake intensity and width vary with Reynolds number and are sensitive to both the roughness elements on the tower and the turbulence intensity in the undisturbed flow. For the high Reynolds numbers appropriate to masts and towers in atmospheric flows, the wake is often nonstationary. Experimental results of different investigators therefore tend to be inconclusive.

In the absence of any firm guidance on the subject, we develop useful rules of thumb. For example, the data can be restricted to a sector that excludes wind directions through the tower and 30° on either side (as a safety factor). For sensors mounted at the end of a boom 1.5 times the tower width, as at the BAO (Fig. 6.18), a 270° sector is then available for useful measurements. Identical instrumentation on booms pointing in opposite directions is essential for full 360° coverage. In many research applications, the investigator can afford to wait for favorable wind directions or confine analyses only to periods when conditions are acceptable.

The amount of reduction in the measured average wind speed 1.5 tower diameters upwind of the tower is typically 5%. The wind direction deflection, on

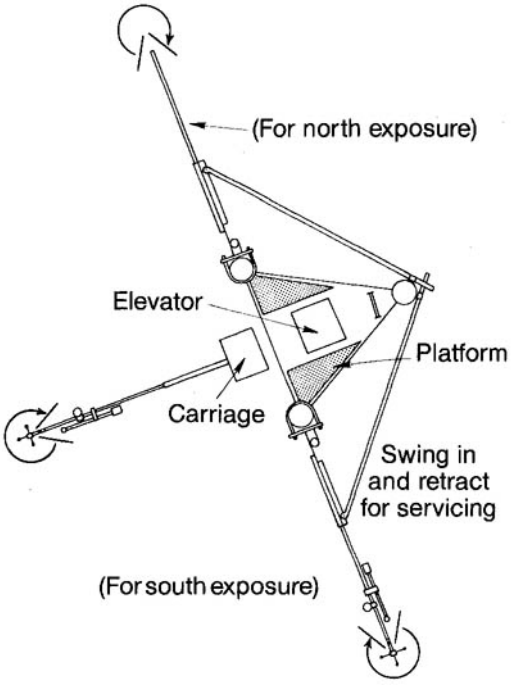

Fig. 6.18 Boom configuration on the Boulder Atmospheric Observatory tower (Kaimal and Gaynor, 1983).

the other hand, is small directly upwind but increases as the wind shifts to either side. The maximum deflection observed on the BAO tower is 5° (at a distance 1.5 times the tower width), for winds normal to the direction of the boom.

The influence of towers on flux measurements must be addressed. Investigators have examined errors in the measured stress from flow distortions caused by boxes stored on tower platforms, by the horizontal booms supporting the sonic anemometer and other sensors, and by the probe itself. Every effort should be made to avoid placement of obstacles above, below, and even downwind of the sensor and to incorporate as much vertical symmetry as possible in the probe design.

If we choose to work in standard Cartesian coordinates, the need for careful alignment of the measurement coordinates with respect to a known reference direction is critical. The momentum flux $(-\overline{u'w'})$ is especially sensitive to leveling errors (Kaimal and Haugen, 1969). Leveling accuracies of $\pm 0.1°$ can be achieved in a sonic anemometer by attaching to each probe an electrolytic level indicator with remote readout. An alternate approach is to analyze data in streamline coordinates as described in Chapter 5. Over complex terrain, this is the preferred choice, but even over nominally homogeneous terrain, working in streamline coordinates can remove the need for exact instrument alignment. (Practical procedures for using this approach will be discussed later in this chapter.) There are some applications (as in strongly distorted flows), however, where it is essential to know the orientation of sensors to an external reference frame.

When mounting two sensors side by side for flux measurements (e.g., vertical velocity and temperature), the spatial separation between them should be kept as small as possible. We find that the fluctuations measured become increasingly uncorrelated at wavelengths $\lambda < 2\pi s$ (where s is the separation distance). Thus the criterion for maximum separation distance is approximately the same as for spatial averaging in individual sensors: $s < \lambda_c/2\pi$, where λ_c is the 98% power point. One attempt to minimize this separation distance and to provide some degree of vertical symmetry in the w measurement is illustrated in Fig. 6.19.

6.5 Measuring in plant canopies

In plant canopies both the spatial heterogeneity and the very high turbulence intensities encountered impose extra constraints on the measurement techniques available.

6.5.1 *Mean velocity*

The very high turbulence intensities in plant canopies ($\sigma_u/\overline{u}$ often as high as 2 or 3) combine with the overspeeding properties of cup anemometers to register a significant and completely spurious mean flow in the lower canopy (Wilson et al.,

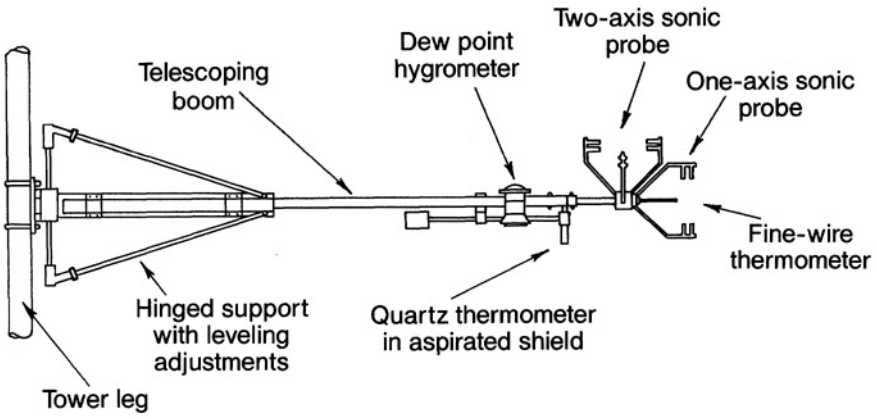

Fig. 6.19 Instrumentation at each observation level and adjustments for leveling the boom on the Boulder Atmospheric Observatory tower (Kaimal and Gaynor, 1983).

1982). Despite this, they remain in regular use in non-critical situations; however, accurate mean velocities are now usually obtained with sonic anemometers.

6.5.2 *Velocity fluctuations*

As in the surface layer over flat terrain, the sonic anemometer is the instrument of choice for measuring velocity fluctuations in a canopy. The effective sampling volumes of most commercial sonic anemometers are small enough for use in forest canopies but too large for smaller crop canopies. A significant portion of the variances and fluxes would be missed. Even in forest canopies, the large amount of small-scale, wake-generated turbulence present dictates the use of probes with the smallest effective path length, such as the CSIRO/Dobbie sonic anemometer. In reasonably dense canopies with plant height 1–2 m or less, even a 5-cm path sonic anemometer may miss significant amounts of the variance. The only small-scale instrument to have met this challenge to date is the servo-driven, split-film anemometer described by Shaw et al. (1973). It must be emphasized, however, that this solution requires considerable technical skill to implement. The research community still awaits a truly miniaturized sonic anemometer to use in plant canopies.

6.5.3 *Scalar fluctuations*

Temperature fluctuations seldom present a problem with thermocouple or platinum wire probes, which can be made very small. The short path length of Lyman-alpha and Krypton hygrometers makes them suitable for use in most canopies, but the longer path of the infrared devices limit their use to larger forest canopies where sonic anemometers may also be used.

6.5.4 *Net radiation*

Within the canopy, absorption of radiation on plant surfaces produces vertical divergence in the net radiation flux R_n. At the same time, the penetration of sunlight through gaps in the foliage makes mandatory some kind of spatial averaging in the R_n measurements. This can be accomplished by moving standard spherical net radiometers on tracks through the canopy or, more conveniently, by using cylindrical net radiometers. These may be several meters long, depending on the particular requirements of the canopy in question. Unlike spherical net radiometers, their response function depends on solar azimuth as well as inclination so that the orientation of the device relative to the sun's position at zenith becomes important. The problems involved are discussed by Lang (1978).

6.5.5 *Ground heat flux*

In forests containing large trees, the energy storage term G_s is no longer associated with the flux into the soil alone but also into the more massive trunks and branches. The term is often estimated from measurements of tree surface temperature and an assumption for the thermal conductivity of the green wood.

In Chapter 3 we emphasized the requirement for spatial averaging in canopies. This means, in practice, that multiple towers may be needed to sample properly the turbulent flow in general and to deduce the dispersive flux in particular. It also means that objective placement of sensors is required if biased samples of the flow are to be avoided. In simple terms, siting every anemometer in a clearing between plants is not acceptable. With objective placement of instruments, some end up in spaces, whereas others are thrust into tree crowns. This is most important in open forests and row crops and least important (also least practical) in dense crop canopies.

Finally, it is useful to remember the pitfalls that exist when standard methods for inferring fluxes from mean gradients are applied too close to the canopy top. Most such techniques rely on assuming equality between the eddy diffusivities for heat, water vapor, and CO_2 (the Bowen ratio method) or between scalars and momentum (the aerodynamic method). In the roughness sublayer above the top of the canopy, these equalities are lost even at neutral stability, as we saw in Chapter 3. Nevertheless, the rapid decrease in scalar gradients, as we move away from the surface, tempts many workers to use these methods in the roughness sublayer, where gradients are large and more easily measured. The literature is littered with the anomalous and inexplicable results of such adventures.

6.6 Measuring over sloping terrain

We have already mentioned the errors that arise in measured fluxes when instruments are not carefully leveled (Section 6.3). To be more precise, problems occur

when vector quantities like velocities or fluxes are measured in a reference framework that does not coincide with that of the equations used to analyze them. In the most familiar case of homogeneous flow over flat ground described in Cartesian coordinates, such difficulties do not occur. In more complex flows, we must be aware of them and deal with them. Two different strategies can be adopted to avoid this problem:

The first is to choose a set of axes that will be used to interpret the measurements, then to align all instruments carefully with the local direction of these axes. A familiar example is the choice of rectangular Cartesian coordinates with the z axis aligned with the geopotential gradient, x in the E-W direction and y in the N-S direction. The difficulties are those of accurately knowing the x, y, z directions at every instrument and aligning the instrument with them. On a single rigid tower such as the BAO, this is the usual choice. In experiments with many instruments mounted on portable towers this strategy is much more difficult to follow.

The second choice is to allow the flow to set the coordinate directions. For example, x may be taken in the direction of the local mean wind vector $\overline{\mathbf{u}}$. The instrument is aligned at its optimum orientation to the prevailing wind and measurements transformed mathematically from the reference frame of the instrument into the chosen frame *after* they have been collected. The use of streamline coordinate equations, recommended in Chapter 5 as the preferred choice for complex terrain studies, relies on this strategy. The problems with this approach are threefold:

1. *Choosing an appropriate set of equations in which to analyze the data.* The streamline coordinate equations are one such set, but in using them we encounter the second problem.
2. *Choosing the direction of the* y *and* z *axes.* (We assume x is taken along a streamline.) In streamline coordinates, y and z are in the directions of the binormal and principal normal to the streamline. To define these directions we need to know how the streamline is varying in space, whereas usually we only have a measurement at a single point. This is a crucial question, and we return to it below.
3. *Knowing the direction of the accelerations due to gravity* $\mathbf{g}$ *relative to the axes of the instrument.* (This may be easier sometimes than aligning the instrument's vertical path with that direction.) If the buoyancy forces are important, we need this information.

The simplest way to illustrate these problems is to go through the steps of producing data in streamline coordinates. Three mathematical transformations are required to get from the instrument's reference frame to the streamline reference frame. We assume that digitally sampled velocity data are recorded in the instrument's rectangular Cartesian reference frame which we denote by x_1, y_1, z_1. The

velocity components in this frame are u_1, v_1, w_1, whereas the components of the acceleration due to gravity vector $\mathbf{g}$ are $g_{x_1}, g_{y_1}, g_{z_1}$.

The first step is to average the time series of velocities to produce a mean wind vector $\overline{\mathbf{u}}$ with components $\overline{u}_1, \overline{v}_1, \overline{w}_1$. It is immediately clear that the mean vector depends upon both the averaging time chosen and the spatial resolution of the instrument. McMillen (1988), in partially adopting the streamline strategy we describe here, used a 200-s running-mean filter to detrend incoming variables and applied a coordinate rotation at the end of each 30-min period.

The first transformation swings the x_1 and y_1 axes around z_1 to produce a new set of axes (x_2, y_2, z_2) with x_2 in the plane spanned by $\overline{\mathbf{u}}$ and z_1 (Fig. 6.20). The new velocity components are given by

$$\begin{aligned} u_2 &= u_1 \cos\theta + v_1 \sin\theta, \\ v_2 &= -u_1 \sin\theta + v_1 \cos\theta, \\ w_2 &= w_1, \end{aligned} \tag{6.11}$$

where

$$\theta = \tan^{-1}\left(\frac{\overline{v}_1}{\overline{u}_1}\right).$$

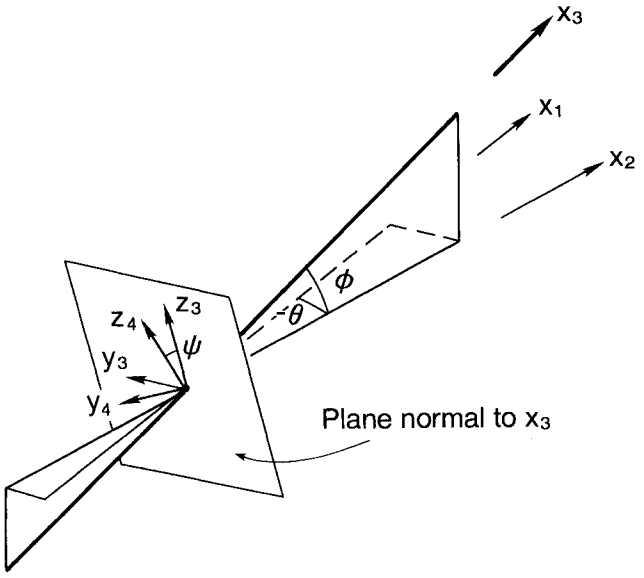

Fig. 6.20 Three-dimensional coordinate rotations for alignment of coordinate axes to the flow field over sloping terrain.

This rotation forces $\overline{v_2} = 0$, but the vertical component is unaffected. The components of the gravity vector become

$$\begin{aligned} g_{x_2} &= g_{x_1} \cos\theta + g_{y_1} \sin\theta, \\ g_{y_2} &= -g_{x_1} \sin\theta + g_{y_1} \cos\theta, \\ g_{z_2} &= g_{z_1}. \end{aligned} \tag{6.12}$$

The second rotation swings x_2 and z_2 about y_2 into new directions x_3, y_3, z_3 so x_3 now points along the mean wind direction (Fig. 6.20). The new velocity components are

$$\begin{aligned} u_3 &= u_2 \cos\phi + w_2 \sin\phi, \\ v_3 &= v_2, \\ w_3 &= -u_2 \sin\phi + w_2 \cos\phi, \end{aligned} \tag{6.13}$$

where

$$\phi = \tan^{-1}\left(\frac{\overline{w}_2}{\overline{u}_2}\right).$$

This rotation forces $\overline{w_3} = 0$. The gravity vector becomes

$$\begin{aligned} g_{x_3} &= g_{x_2} \cos\phi + g_{z_2} \sin\phi, \\ g_{y_3} &= g_{y_2}, \\ g_{z_3} &= -g_{x_2} \sin\phi + g_{z_2} \cos\phi. \end{aligned} \tag{6.14}$$

At this point the x_3 axis points in the direction of the mean wind vector, but the directions of the y_3 and z_3 axes depend on the initial choice of instrument alignment. Before we decide on a means to define the y and z directions, we must discuss the physical basis for the choice of axes in streamline coordinates.

In Chapter 5 we pointed out that the z axis in streamline coordinates points in the direction in which the streamline is curving most rapidly, the principal normal direction. In two-dimensional flows, as in winds blowing normal to a ridge, the principal normal direction is always perpendicular to the stream surfaces and so is the natural generalization of the z direction over flat ground. This is true for axially symmetric flows also, but in three-dimensional flow the behavior of stream surfaces is often much more complicated. In fact, the stream function, whose constant surfaces are the stream surfaces, does not exist in three dimensions except in some restricted types of flows.

In principle, we could identify a stream surface over flat ground somewhere upwind of our observing site and follow it as it is distorted over a hill, keeping our z_3 direction normal to its surface. In practice this is impossible. Instead we continue to identify the z_3 direction with the principal normal. We do this for two reasons: first, for compatibility with the simpler two-dimensional case; second, and more fundamentally, because this choice is what forces the canonical separation of the momentum equation in streamline coordinates into equations for linear and angular momentum.

The principal normal direction is defined by the spatial rate of change of $\mathbf{t}$, the unit tangent to the streamline as we move a distance s along the streamline. This dependence is expressed in the Serret-Frenet formula:

$$\frac{d\mathbf{t}}{ds} = \frac{\mathbf{n}}{R}, \tag{6.15}$$

where $\mathbf{t} = \overline{\mathbf{u}}/|\overline{\mathbf{u}}|$, $\mathbf{n}$ is the unit vector in the principal normal direction, and R is the local radius of streamline curvature. Equation (6.15) can be rewritten in terms of derivatives taken in the Cartesian reference frame of the instrument (x_1, y_1, z_1) but to do this would not be helpful since a single instrument does not provide the information on the spatial gradients of the velocity field necessary to deduce the components of $\mathbf{n}$ from (6.15).

We are, however, familiar with one means of connecting spatial velocity gradients with single point measurement, that is, by an eddy diffusivity. In rectangular Cartesian coordinates the connection between the mean strain and turbulent stress tensors through an eddy diffusivity K can be written as

$$\overline{u_i' u_j'} - \frac{1}{3}\overline{u_i' u_i'} = -\frac{K}{2}\left(\frac{\partial \overline{u}_i}{\partial x_j} + \frac{\partial \overline{u}_j}{\partial x_i}\right). \tag{6.16}$$

If we transform the off-diagonal $(i \neq j)$ components of (6.16) into streamline coordinates, we obtain

$$\overline{u'w'} = -K\left(\frac{d\overline{\mathbf{u}}}{dz} + \frac{\overline{\mathbf{u}}}{R}\right), \tag{6.17a}$$

$$\overline{v'w'} = -KC_{123}, \tag{6.17b}$$

$$\overline{u'v'} = -K\frac{d\overline{\mathbf{u}}}{dy}. \tag{6.17c}$$

The quantity C_{123} that appears in (6.17b) is called the commutator of the field of streamlines. It is a measure of the degree that streamlines twist as well as curve. It is zero in two-dimensional and axially symmetric flow fields and on the

centerline of axially symmetric hills because streamlines are plane curves in these situations. It is likely to be very small close to the surface over low topography, which we might define as hills that are gentle enough to avoid separation. In fact, it is a reasonable rule of thumb that C_{123} will be negligible in any region where we can apply the modified surface similarity theory proposed for use over hills in Chapter 5, Section 5.4. We should, however, be wary of assuming $C_{123} = 0$ over steep topography, on the flanks of axially symmetric hills, or far from the surface in any kind of three-dimensional complex terrain.

With these caveats, we see that, if $C_{123} = 0$ and an eddy diffusivity can be used (its actual form is immaterial), equation (6.17b) provides a means of choosing the z direction; we simply rotate the y_3, z_3 axes around x_3 until $\overline{v'w'} = 0$, as indicated in Fig. 6.19. The new velocity components are

$$\begin{aligned} u_4 &= u_3, \\ v_4 &= v_3 \cos\psi + w_3 \sin\psi, \\ w_4 &= -v_3 \sin\psi + w_3 \cos\psi, \end{aligned} \tag{6.18}$$

where

$$\psi = \frac{1}{2} \tan^{-1} \left[\frac{2\overline{v_3 w_3}}{(\overline{v_3^2} - \overline{w_3^2})} \right].$$

If $\overline{v_2 w_2} = 0$, no rotation is needed. If $\overline{v_2^2} = \overline{w_2^2}$, we have $\psi = 45°$. The components of the gravity vector become

$$\begin{aligned} g_{x_4} &= g_{x_3}, \\ g_{y_4} &= g_{y_3} \cos\psi + g_{z_3} \sin\psi, \\ g_{z_4} &= -g_{y_3} \sin\psi + g_{z_3} \cos\psi. \end{aligned} \tag{6.19}$$

Two notes of caution must be sounded at this point. Typical run-to-run variations in measured $\overline{v_3' w_3'}$ from any of the causes discussed in Chapter 7 may lead to apparently erratic behavior in the direction of the z axis. Careful choice of smoothing filters may be necessary to rectify this. Second, rotating into streamline coordinates does not mean that momentum transfer in the y direction vanishes. Equation (6.17c) demonstrates this even for the restrictive case where an eddy diffusivity may be used.

In situations where we cannot assume that K exists and $C_{123} = 0$, there is no alternative to direct measurement of the spatial variation in the velocity

field. In such situations it is tempting to choose the z direction arbitrarily. For example, it could be taken as lying in the plane containing $\overline{\mathbf{u}}$ and $\mathbf{g}$. It must be emphasized, however, that data collected in such a reference frame would not form the dependent variables of the streamline coordinate equations and a new set of equations would have to be derived in order to perform the analysis. Such equations would be linear combinations of the streamwise and cross-stream momentum equations but the interpretive power of the streamline equations, for which $(\overline{u}_4 + u'_4), v'_4$, and w'_4 are automatically the dependent variables, would be lost.

In order to apply streamline coordinate analysis, the important length scales L_a and R must be deduced. The acceleration length scale L_a can be inferred if velocity data from a series of masts are available. See, for example, Finnigan and Bradley (1983). Close to the surface, it is usually reasonable to take $R = R_0 + z$, where R_0 is the surface curvature. This could be measured directly by surveyor's methods or, on the large scale, deduced from a contour map. It is not advisable to attempt to deduce R from (6.17a).

To summarize, over gentle hills or close to the surface on steeper topography, as long as separation regions are avoided, working in streamline coordinates can avoid the necessity of accurately aligning anemometers relative to some external reference frame. In flows with complex distortions, although streamline coordinates may still be the preferred choice for analysis, information on the spatial evolution of the flow is required to fix the coordinate directions and to deduce the curvature and acceleration length scales. In such cases the relative orientation of the sensors, at least, must be accurately known. It is worth noting that most surface layer analyses undertaken to date fall into the first category; very few field experiments dealing with strongly distorted flows, as defined above, have yet been attempted.

6.7 In situ measurements above tower heights

Extending measurements made near the ground with in situ sensors into the upper boundary layer is by no means a simple task. The techniques available for reaching those heights to measure mean winds, temperatures, and humidities are many. They include free balloons, tethered balloons, kytoons (inflatable kites), aircraft, and drones. Measuring fluxes and variances above tower heights poses an even greater challenge. The difficulty arises because turbulence measurements require stable platforms and precise leveling for best results. Two techniques have so far provided dependable turbulence data above 100 m, but they are both costly and complex and involve specialized equipment and trained personnel to operate them. In one, the tethering cable of a very large balloon is used to suspend sensors at different heights (Caughey and Palmer, 1979; Readings et al., 1974). In the

other, an aircraft is instrumented for level flights at different heights over the site (Lenschow et al., 1980; Nicholls and Readings, 1981).

The tethering cable of a large balloon offers the closest approximation to a tall tower. Barrage balloons of the type used in the Minnesota experiment (Readings et al., 1974) are ideal for this purpose, being capable of ascents up to 3 km with large payloads. This type of balloon is relatively insensitive to turbulent fluctuations in the wind but does oscillate laterally as it hovers downwind of the tethering point. The oscillation, although very slow (5–10-min period), introduces overestimations in the measured wind speed ($\sim$10%) and its variance ($\sim$30%) without seriously affecting the vertical velocity and temperature variances or even the fluxes of momentum and heat (Haugen et al., 1975). The turbulence probe has to be specially designed to maintain its verticality and orientation to the wind while attached to the tethering cable.

The instrumented aircraft measures the spatial-temporal distribution of variables which differs from the temporal measurements obtained from sensors on the balloon cable. (If the aircraft speed U is large compared with the turbulent velocity scales, we can use Taylor's hypothesis, writing $\kappa_1 = 2\pi f/U$.) The aircraft can probe the entire depth of the CBL above 50 m in less than 2 h, flying in combined horizontal- and vertical-profiling modes. The aircraft itself, however, responds to turbulent motions, and this contamination has to be measured accurately and removed from the data. Sensors for measuring wind, temperature, and humidity fluctuations are usually mounted on specially designed booms or supports on the front of the aircraft. These sensors have to respond more rapidly to the fluctuations than their counterparts on balloon cables because aircraft speeds are higher than eddy translation speeds in the boundary layer. Corrections also need to be applied for compressibility and aircraft flow distortion effects on the measurements. These corrections complicate subsequent analysis of the aircraft data. Details of the instrumentation and the various corrections applied to the measurements are described by Lenschow (1986). Accuracies of 10% in the second moments can be achieved with flight legs of 20 min (80–120 km) or more.

6.8 Remote sensors for the boundary layer

Remote sensors are now used increasingly in boundary layer experiments. They have the range to get above tower heights, but their accuracies and spatial resolutions are still too coarse for detailed turbulence work. Turbulence parameters such as C_T^2, C_V^2 and the fluxes of heat and momentum can be inferred indirectly from backscattered and forward-propagated signals with varying degrees of accuracy. In many applications they are valued for the broad spatial coverage they offer in the forms of vertical profiles of winds and temperatures; for time-height plots showing evolution of such features as the daytime capping inversion, gravity waves, elevated inversion layers, and SBL depths; and for flow fields over com-

plicated terrain. Such remote sensors fall into three major categories depending on the type of signal used and are commonly referred to as sodars, radars, and lidars, acronyms for *so*und, *ra*dio, and *li*ght *d*etection *a*nd *r*anging, respectively.

6.8.1 *Sodars*

The standard Doppler sodar, operating at frequencies around 2 kHz, is available in different versions from several manufacturers. In its monostatic version, the sodar measures radial wind components along three narrow beams, one pointing vertically and two tilted 30° (typically) from zenith pointing E (or W) and N (or S). The wind components are derived from Doppler shifts measured in the backscattered sound pulses transmitted sequentially in the three directions. (Each antenna switches from transmitting to receiving mode to sense the back-scattered signal.) The three beams may be produced either from three separate collocated antennas or from a phased array of transducers that steer the beam electronically into those directions. The range resolution for such a sodar (i.e., the length of the acoustic pulse transmitted) is typically 30 m over a height range 50–500 m. (Radial velocities measured along the two tilted beams are converted into horizontal components along the cardinal directions.) The minimum cycling time for one set of transmissions is typically 6 s; the minimum averaging time for a reliable estimate of the radial wind component is 6 min. Expected accuracy in these sodars is ± 1 m s^{-1}.

Doppler minisodars operating in the 5–8-kHz range, with similar antenna options, claim better accuracies ($\pm$ 0.5 m s^{-1}), better range resolutions ($\sim$10 m), shorter averaging times ($\sim$1 min), and greatly reduced operating range (10–200 m). Only a few research versions exist (Coulter, 1990). Because of their small size and portability, they can be placed in difficult-to-reach locations; their low cost and short range permit deployment of several units in the same area for studies of complicated flows within valleys and on sloping terrain.

Time-height facsimile records of the monostatic echo intensities, familiar to sodar enthusiasts for over two decades, provide useful records of temperature structures in the ABL and their evolution with time. In the monostatic mode these backscattered signals are produced entirely by temperature inhomogeneities (C_T^2). Many ABL structures [e.g., convective plumes, waves, gust fronts, capping inversions, and ground-based stable turbulent layers (used often as an indicator of SBL depth)] contain temperature inhomogeneities that scatter sound, and each can be identified by its own special signature (Neff and Coulter, 1985). Because of the sodar's limited maximum range, the capping inversion can be tracked through only part of its rise, until about 1000 local time on most days.

In the bistatic mode (in which separate tilted transmitter and receiver beams intersect at designated heights above ground), scattering is produced primarily by velocity inhomogeneities (C_V^2); the contribution from C_T^2, usually two orders of

magnitude smaller, is ignored (Thomson et al., 1978). Bistatic Doppler systems (e.g., Kaimal and Haugen, 1977), common a decade ago, need more area on the ground than the monostatic systems to accommodate their widely separated antennas and, moreover, perform less well. The trend today is toward increasingly compact transducer groupings, such as multiple monostatic antennas and phased arrays.

6.8.2 *Radar*

Doppler wind profiling radars operating at UHF (915 and 404 MHz) and VHF (50 MHz) frequencies currently used for monitoring winds in the troposphere (Frisch et al., 1986; Strauch et al., 1984), have minimum ranges that are too high ($\sim$1 km) for boundary layer measurements. The new 915-MHz boundary layer profiler described by Ecklund et al. (1988), with its highly portable (0.9 $\times$ 0.9 m) microstrip antenna panels and compact electronics, appears, however, ideally suited for that application. It has a height resolution of $\sim$50 m, a minimum range of $\sim$100 m, and a maximum range conservatively rated at 1.5 km. It adequately covers the CBL depth except under very dry conditions when moisture fluctuations also happen to be very low. In a moist environment, the maximum range can be as high as 4.5 km.

Like monostatic Doppler sodars, these radar wind profilers are ground-based, three-beam systems: one beam vertical and two tilted 15° from zenith in the N (or S) and E (or W) directions. The antennas are pulsed rapidly ($\sim$100-μs repetition rate), the propagation speed being much higher for the electromagnetic wave than for sound. This rapid sampling is necessary because the signal-to-noise ratio in radar returns is very low compared to sodars, and a large number of samples is needed to achieve comparable accuracy. Typically, a single reading from any range gate (time gate corresponding to calculated range interval along the beam) is an average of $\sim$ 150,000 successive returns (transmission every 100 μs for, say, 15 s). Counting the time needed for switching between antennas, the total cycling time for one sequence of data points is about 1 min. A minimum of 20 such data points is needed to construct a wind profile accurate to within $\pm$0.5 m s^{-1}.

The strongest radar returns are predominantly from refractive index variations of scale size $\lambda/2$, where λ is the radar wavelength (33 cm at 915 MHz). If the $\lambda/2$ scale sizes are in the inertial subrange of the turbulence spectrum, the radar reflectivity is given by 0.38 $C_n^2\lambda^{-1/3}$ (Ottersten, 1969). (C_n^2 is the refractive index structure parameter mentioned in Chapter 2.) The abrupt drop observed in backscatter intensity above the CBL is attributed to a sharp attenuation of turbulent energy in the $\lambda/2$ scale sizes in the relatively smooth flow in that region. Lack of moisture also plays a role. For radar signals, C_n^2 is most strongly influenced by C_Q^2, with lesser contributions from C_T^2 and C_{TQ}. This new term, C_{TQ}, is the

structure parameter derived from the temperature-humidity cospectrum (Friehe et al., 1975) through the relationship:

$$C_{\theta q}(\kappa_1) = 0.25\, C_{TQ}\, \kappa_1^{-5/3}. \tag{6.20}$$

The C_{TQ} contribution may be positive or negative, depending on the sign of the correlation between temperature and humidity, so it could either enhance or diminish C_n^2. In any case, radar reflectivity drops off abruptly at the top of the CBL, and the level where this drop begins can, under ideal conditions, be used as a measure of z_i.

6.8.3 *Lidars*

Pulsed Doppler lidars are optical analogs of the more familiar Doppler radars. The lidar's shorter wavelength makes it sensitive to aerosols and cloud particles that follow air motions well and therefore serve as good targets for wind sensing. The aerosol loading in the boundary layer is usually sufficient for many lidars to operate with good signal-to-noise ratio. This ratio can drop to very low values above the CBL if the air is very "clean." Obscurants like smoke will also limit its range, whereas thick fog and clouds could block it entirely.

The lidar can be deployed in a three-beam mode as in radar wind profilers. It is, however, most effectively used in the velocity azimuth display (VAD) mode making conical scans through 360° azimuth at constant elevation angle (say 30°). The lidar beam has no side lobes and therefore suffers no complication from ground clutter, except for direct strikes. The CO_2 Doppler lidar, operating in the infrared (10.6 μm), is ideal for wind profiling. It is eyesafe and can therefore be used in field experiments to provide low-angle conical and elevation scans of the wind field over a 10-km horizontal range. In the VAD mode, the radial winds in each range gate execute a sinusoidal pattern as the beam moves through its conical scan. The azimuth of the velocity peak yields the wind direction and the amplitude of the peak, the speed. This assumes that the flow is horizontally homogeneous. The range resolution is poor (~300 m) because of the minimum record length needed for Doppler processing; however, at shallow scan angles this range resolution would translate to much better height resolutions.

The lidar may also be used as an indicator of z_i. The top of the CBL is often clearly delineated in lidar backscatter displays because of strong aerosol gradients in that region. C_n^2 for optical waves is produced primarily by C_T^2, with much smaller contributions from C_Q^2 and C_{TQ} (Friehe et al., 1975). Nevertheless, the C_T^2 maximum at z_i (Chapter 2), although strong enough to be identified in the sodar returns, is not apparent in lidar plots.

Present CO_2 lidars operating in the Doppler mode are large, complicated systems (Hardesty, 1984). They have proved valuable in complex terrain studies,

especially for mapping flows through canyons. Because of their complexity and high operating cost, they are seldom available for low-budget boundary layer studies. Doppler lidar technology is, however, rapidly moving toward less expensive, more compact, and more robust systems with hopes also for better accuracy and resolution; when those systems are developed, we can expect to see lidars used more widely in boundary layer experiments.

6.8.4 *Radio acoustic sounding system*

Radio Acoustic Sounding System (RASS) combines both radar and acoustic techniques to sense temperature profiles remotely. The concept is not new, but it was not widely used in the United States until the arrival of sensitive Doppler radar systems (such as those developed for wind profiling). These new radars are capable of tracking Doppler shifts in the weak signals scattered back from radar refractive index undulations induced by sound waves propagating upward from a source near the radar. The Doppler shift in the signal is a measure of the speed of sound, which is directly related to the virtual temperature, T_v. [From our definitions in (6.3) and (6.10), we have $c^2 \simeq 403T_v$.] The heights of observation would be those corresponding to the radar range gates where the receding refractive index undulations (accompanying the sound) provide strong enough returns for Doppler processing.

Strong backscattered signals are obtained when the wavelength of the transmitted acoustic signal is matched to half the radar wavelength (the Bragg condition) and the radar and acoustic phase fronts are matched. For the 915-MHz radar, the matching acoustic frequency is $\sim$2 kHz at temperatures typically encountered in the ABL. But exact matching is difficult to achieve with a fixed frequency acoustic source, given the spatial and temporal temperature variabilities in the ABL. So a frequency-modulated, continuous-wave (FM-CW) acoustic signal is transmitted (upward) to ensure Bragg match with the radar at all heights that give a detectable radar signal. The range gates where both Bragg match and phase match are achieved, and where the T_v readings are the most reliable, would vary from one radar scan to the next. However, the temperature readings thus obtained, when consolidated, yield profiles with fine details that include sharp inversions (Currier et al., 1988; May et al., 1990) that compare very well (within $\pm 1°$C) with radiosonde data.

In all RASS systems (404- and 50-MHz systems included), the maximum range achieved is limited by strong winds that advect the acoustic wavefronts so they no longer match the radar wavefronts, by turbulence and temperature gradients that distort the acoustic wavefronts, and by acoustic attenuation. In the 915-MHz RASS, acoustic absorption is particularly serious. The maximum range of this RASS system is typically 750 m, although observations have been reported up to 1.2 km in moist air (Currier et al., 1988). The presence of moisture

enhances RASS performance because acoustic absorption in the 2-kHz range (at temperatures encountered in the ABL) decreases with increasing humidity. The height resolution and minimum range for RASS are the same as for the 915-MHz wind profiler, ~50 m and ~100 m, respectively.

6.9 Special symbols

a	transducer diameter
c	velocity of sound in air
C_{123}	commutator of the field of streamlines
E	voltage across bridge
g_x, g_y, g_z	components of gravity vector along x, y, z directions
$\mathbf{g}$	gravity vector
$H(\lambda)$	power transfer function, function of λ
l	distance constant of anemometer
L_a	acceleration length scale
M_a, M_w	molecular weights for air and water vapor
$\mathbf{n}$	unit vector in the principal normal direction
p_d	dynamic pressure
R	local radius of curvature of streamline
R_0	surface curvature
s	separation distance
s	distance along streamline
$\mathbf{t}$	unit tangent vector to a streamline
t_1, t_2	sonic anemometer transit times
u_p	local pressure variation caused by the pressure probe
$\overline{\mathbf{u}}$	local mean wind vector
U	aircraft speed
V_d	velocity component along acoustic path d
V_n	velocity component normal to V_d
V_o	bridge output in volts
V_A, V_B	velocity components along nonorthogonal sonic anemometer axes, A and B
V_H	horizontal wind vector
V_X, V_Y	velocity components along orthogonal sonic anemometer horizontal axes, X and Y
γ_a, γ_w	ratio of specific heats for air and water vapor
θ	azimuth angle
λ_c	cutoff wavelength
λ_0	half-power wavelength
ϕ	elevation angle
ψ	angle of coordinate rotation around the $\overline{\mathbf{u}}$ direction

Appendix 6.1 Principle of the sonic anemometer and thermometer

The sonic anemometer measures wind components from transit times of acoustic signals traveling in opposite directions along a fixed path. Figure 6.21 illustrates the effect of wind V on the sound ray vectors for a single-axis anemometer. If t_1 and t_2 are the transit times for pulses traveling along wind directions defined positive and negative, respectively, we have

$$t_1 = \frac{d}{(c\cos\gamma - V_d)}, \tag{6.21}$$

$$t_2 = \frac{d}{(c\cos\gamma + V_d)}, \tag{6.22}$$

where d is the path length, c is the velocity of sound, V_d is the wind component along the path, and $\gamma = \sin^{-1}(V_n/c)$, V_n being the component normal to the path.

Two methods are used to extract V_d. One, which involves measuring $(t_1 - t_2)$, is simpler to implement if the pulses travel simultaneously along two close, but separate, parallel paths. The measurement has a residual temperature sensitivity, which, although small, cannot be ignored. Assuming $V_n^2 \ll c^2$, we have

$$\begin{aligned} t_2 - t_1 &= \frac{2d}{c^2} V_d \\ &\simeq \left[\frac{2d}{403T(1 + 0.32e/p)}\right] V_d \\ &\approx \left(\frac{d}{201.5T_v}\right) V_d, \end{aligned} \tag{6.23}$$

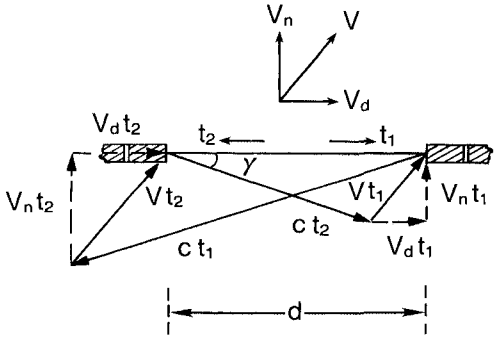

FIG. 6.21 Sound ray vectors for a single-axis, single-path sonic anemometer.

on substituting for c^2 from (6.3) and assuming $T(1 + 0.32e/p)$ is an adequate approximation of the virtual temperature T_v [defined as $T(1 + 0.38e/p)$]. The error involved in assuming the measured temperature equals T_v is on the order of 0.01°C (Kaimal and Gaynor, 1991), well within the bounds of experimental uncertainty. [The difference arises from the fact that the coefficient of e/p in the expression for T_v is $(1 - M_w/M_a)$, where M_w and M_a are the molecular weights for water vapor and air, whereas that for the sonic-derived temperature is $(\gamma_w/\gamma_a - M_w/M_a)$, where γ_w and γ_a are the ratio of specific heats for water vapor and air.]

The other method computes the reciprocals of t_1 and t_2 to give

$$\frac{1}{t_1} - \frac{1}{t_2} = \frac{2}{d} V_d, \tag{6.24}$$

or

$$V_d = \frac{d}{2}\left(\frac{1}{t_1} - \frac{1}{t_2}\right), \tag{6.25}$$

which is free of any temperature sensitivity. This approach is implemented in the newer single-path sonic anemometers that transmit signals back and forth sequentially along the same path and measure t_1 and t_2 separately, instead of the difference between them.

Sonic thermometry benefits as well from the separate determinations of t_1 and t_2. We can write

$$\begin{aligned} \frac{1}{t_1} + \frac{1}{t_2} &= \frac{2}{d} c \cos\gamma \\ &= \frac{2}{d}(c^2 - V_n^2)^{1/2} \end{aligned} \tag{6.26}$$

or

$$c^2 = \frac{d^2}{4}\left(\frac{1}{t_1} + \frac{1}{t_2}\right)^2 + V_n^2. \tag{6.27}$$

Substituting for c^2 from (6.3) and assuming again that the temperature derived from the speed of sound approximates T_v, (6.21) becomes

$$T_v = \frac{d^2}{1612}\left(\frac{1}{t_1} + \frac{1}{t_2}\right)^2 + \frac{1}{403} V_n^2. \tag{6.28}$$

If $1/t_1$ and $1/t_2$ are determined from the w axis of the sonic anemometer, V_n would be the magnitude of the horizontal wind vector V_H.

In the orthogonal array of Fig. 6.9,

$$V_n^2 = V_X^2 + V_Y^2, \tag{6.29}$$

where V_X and V_Y are wind components measured along the horizontal X and Y axes, corrected for transducer shadowing as described in Appendix 6.3.

Appendix 6.2 Nonorthogonal array

In an orthogonal array (e.g., Fig. 6.9), coordinate transformation to resolve the horizontal wind components is fairly straightforward. For the nonorthogonal 120° array (Fig. 6.8), however, the transformation involves more terms. If V_A and V_B are the velocities measured along the horizontal axes A and B (Fig. 6.22) and u and v are the velocity components along the vector mean coordinates,

$$u = V_A\left(\cos\theta - \frac{1}{\sqrt{3}}\sin\theta\right) + V_B\left(\cos\theta + \frac{1}{\sqrt{3}}\sin\theta\right), \tag{6.30}$$

$$v = -V_A\left(\frac{1}{\sqrt{3}}\cos\theta + \sin\theta\right) + V_B\left(\frac{1}{\sqrt{3}}\cos\theta - \sin\theta\right), \tag{6.31}$$

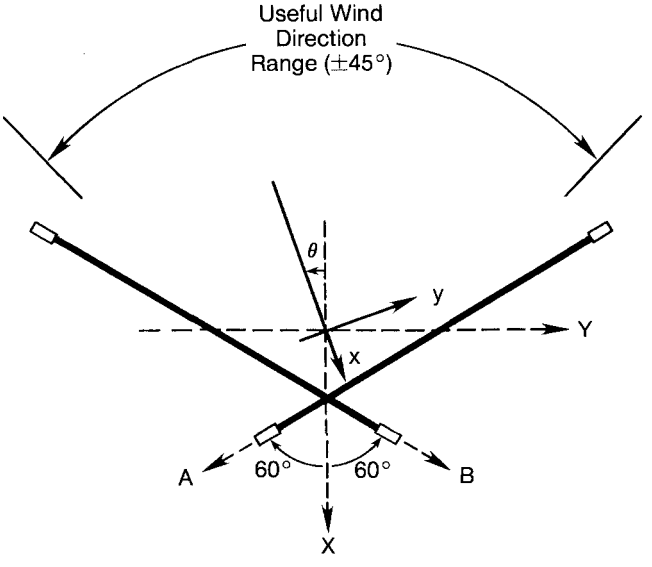

Fig. 6.22 Horizontal vector-mean wind coordinates (x, y) and nonorthogonal sonic anemometer axes (A, B).

where

$$\theta = \tan^{-1}\left[\frac{\overline{V}_B - \overline{V}_A}{\sqrt{3}(\overline{V}_B + \overline{V}_A)}\right],$$

where θ is the angle between the horizontal wind vector and the axis of symmetry of the array.

Appendix 6.3 Correction for transducer shadowing

In the orthogonal array of Fig. 6.9, partial shadowing of the acoustic path by the transducers causes the velocity readings to be underestimated. Results of wind tunnel and atmospheric tests indicate a linear drop in response as the wind direction approaches the direction of the acoustic path. The degree of attenuation is a strong function of the aspect ratio d/a for $d/a < 50$, where d is the path length and a the diameter of the transducer (Fig. 6.23). The measured velocity component $(V_d)_m$ for $d/a = 15$ becomes

$$(V_d)_m = \begin{cases} V_d(0.82 + 0.18\theta/75), & 0° \leq \theta \leq 75° \\ V_d, & 75° \leq \theta \leq 90°, \end{cases} \tag{6.32}$$

where

$$\theta = \cos^{-1}\left(\frac{|V_d|}{|V_H|}\right).$$

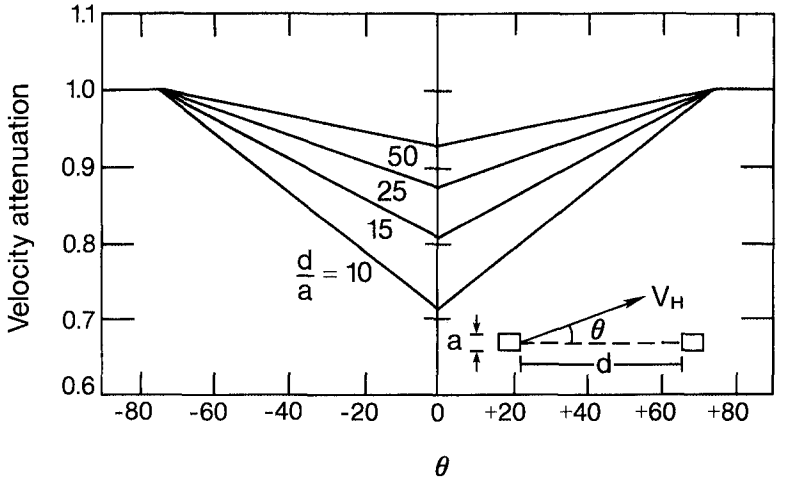

FIG. 6.23 Velocity attenuation from transducer shadowing in a sonic anemometer shown as a function of wind direction for various values of d/a.

θ is the angle between V_d and the horizontal wind vector V_H. The attenuation for d/a other than 15 can be estimated from the curves in Fig. 6.19. Note that Fig. 6.19 represents the shadow effect produced by the Applied Technologies' 1-cm diameter $\times$ 1-cm long transducer mounted at the end of a short 1-cm diameter transducer holder (Fig. 6.9). The shapes will be different for other types of transducers and mounts (Kaijo Denki and CSIRO/Dobbie arrays), as pointed out by Wyngaard and Zhang (1985).

References

Andreae, M. O., and D. S. Schimel, 1989: Exchange of trace gases between terrestrial ecosystems and the atmosphere, Report of the Dahlem Workshop, 19-24 February 1989, Berlin, Germany, Wiley-Interscience, New York, 346 pp.

Buck, A. L., 1976: A variable path Lyman-alpha hygrometer and its operating characteristics. *Bull. Amer. Meteor. Soc., 57*, 1113–1118.

Busch, N. E., O. Christensen, L. Kristensen, L. Lading, and S. E. Larsen, 1980: Cups, vanes, propellers and laser anemometers. In *Air-Sea Interaction—Instruments and Methods.* Plenum Press, New York, 11–46.

Caughey, S. J., and S. G. Palmer, 1979: Some aspects of turbulence structure through the depth of the convective boundary layer. *Quart. J. Roy. Meteor. Soc., 105*, 811–827.

Coppin, P. A., and K. J. Taylor, 1983: A three-component sonic anemometer/thermometer system for general micrometeorological research. *Bound.-Layer Meteor., 27*, 27–42.

Coulter, R. L., 1990: Minisodars—Applications and potential. In *Acoustic Remote Sensing* (S. P. Singal, Ed.), Tata McGraw-Hill, New Delhi, 88–96.

Currier, P. E., W. L. Ecklund, D. A. Carter, J. M. Warnock, and B. B. Balsley, 1988: Temperature profiling using a UHF wind profiler and an acoustic source. *Extended Abstracts, Lower Tropospheric Profiling—Needs and Technologies*, May 31–June 3, 1988, Boulder, CO; American Meteorological Society, Boston, MA, 121–122.

deVries, D. A., and J. R. Philip, 1986: Soil heat flux, thermal conductivity, and the null alignment method. *Soil Sci. Soc. Am. J., 50*, 12–18.

Dunin, F. X., W. Reyenga, and I. C. McIlroy, 1991: Australian lysimeter studies of field evaporation, *Proc. International Symp. on Lysimetry* (R. G. Allen, T. A. Howell, W. O. Pruitt, I. A. Walter, and M. E. Jensen, Eds.), 23-25 July 1991, IR Div./ASCE, Honolulu, HI, 237–245.

Ecklund, W. L., D. A. Carter, and B. B. Balsley, 1988: A UHF wind profiler for the boundary layer: Brief description and initial results. *J. Atmos. Oceanic Tech., 5*, 432–441.

Elliott, W. P., 1972: Instrumentation for measuring static pressure fluctuations within the atmospheric boundary layer. *Bound.-Layer Meteor., 2* , 476–495.

Finkelstein, P. L., J. C. Kaimal, J. E. Gaynor, M. E. Graves, and T. J. Lockhart, 1986: Comparison of wind monitoring systems. Part I. In situ sensors. *J. Atmos. Oceanic Tech., 3* , 583–593.

Finnigan, J. J., and E. F. Bradley, 1983: The turbulent kinetic energy budget behind a porous barrier: An analysis in streamline coordinates. *J. Wind Eng. Ind. Aerodyn., 15*, 157–168.

Friehe, C. A., J. C. LaRue, F. H. Champagne, C. H. Gibson, and C. F. Dreyer, 1975: Effects of temperature and humidity fluctuations on the optical refractive index in the marine boundary layer. *J. Opt. Soc., 65*, 1502–1511.

Frisch, A. S., B. L. Weber, R. G. Strauch, D. A. Merritt, and K. P. Moran, 1986: The altitude coverage of the Colorado wind profilers at 50, 405, and 915 MHz. *J. Atmos. Oceanic Tech., 3*, 680–692.

Grant, A. L. M., and R. D. Watkins, 1989: Errors in turbulence measurements with a sonic anemometer. *Bound.-Layer Meteor., 46* , 181–194.

Hanafusa, T., Y. Kobori, and Y. Mitsuta, 1980: Single head sonic anemometer-thermometer. In *Instruments and Observing Methods, Report No. 3*, World Meteorological Organization, Geneva, Switzerland, 7–13.

Hardesty, R.M., 1984: Coherent DIAL measurements of range-resolved water vapor concentration. *Appl. Optics, 23*, 2545–2553.

Haugen, D. A., J. C. Kaimal, C. J. Readings, and R. Rayment, 1975: A comparison of balloon-borne and tower-mounted instrumentation for probing the atmospheric boundary layer. *J. Appl. Meteor., 14*, 540–545.

Horst, T. W., 1973: Corrections for response errors in a three-component propeller anemometer. *J. Appl. Meteor., 12*, 716–725.

Kaimal, J. C., 1969: Measurement of momentum and heat flux variations in the surface boundary layer. *Radio Sci., 4*, 1147–1153.

Kaimal, J. C., and J. E. Gaynor, 1983: The Boulder Atmospheric Observatory. *J. Clim. Appl. Meteor., 22*, 863–880.

Kaimal, J. C., and J. E. Gaynor, 1991: Another look at sonic thermometry. *Bound.-Layer Meteor., 56*, 401–410.

Kaimal, J. C., and D. A. Haugen, 1969: Some errors in the measurement of Reynolds stress. *J. Appl. Meteor., 8*, 460–462.

Kaimal, J. C., and D. A. Haugen, 1977: An acoustic Doppler sounder for measuring wind profiles in the lower boundary layer. *J. Appl. Meteor., 16*, 1298–1305.

Kaimal, J. C., J. C. Wyngaard, and D. A. Haugen, 1968: Deriving power spectra from a three-component sonic anemometer. *J. Appl. Meteor., 7*, 827–837.

Kaimal, J. C., J. E. Gaynor, H. A. Zimmerman, and G. A. Zimmerman, 1990: Minimizing flow distortion errors in a sonic anemometer. *Bound.-Layer Meteor., 53*, 103–115.

Lang, A. R. G., 1978: Note on the cosine response of cylindrical net radiometers. *Agric. Meteor., 19*, 391–397.

Lenschow, D. H., 1986: Aircraft measurements in the boundary layer. In *Probing the Atmospheric Boundary Layer*, American Meteorological Society, Boston, MA, 39–55.

Lenschow, D. H., J. C. Wyngaard, and W. T. Pennell, 1980: Mean-field and second-moment budgets in a baroclinic, convective boundary layer. *J. Atmos. Sci., 37*, 1313–1326.

Lynch, R. A., and E. F. Bradley, 1972: Shearing stress meter. *J. Appl. Meteor., 13*, 588–591.

May, P. T., R. G. Strauch, K. P. Moran, and W. L. Ecklund, 1990: Temperature sounding by RASS with wind profiler radars: A preliminary study. *IEEE Trans. Geosci. Remote Sens., 28*, 19–28.

McMillen, R. T., 1988: An eddy correlation technique with extended applicability to non-simple terrain. *Bound.-Layer Meteor. , 43*, 231–245.

Monteith, J. L., 1975: *Vegetation and the Atmosphere, Vol. 1. Principles.* Academic Press, New York, 278 pp.

Monteith, J. L., 1976: *Vegetation and the Atmosphere, Vol. 2. Case studies.* Academic Press, New York, 439 pp.

Neff, W. D., and R. L. Coulter, 1985: Acoustic remote sensing. In *Probing the Atmospheric Boundary Layer*, American Meteorological Society, Boston, MA, 201–239.

Nicholls, S., and C. J. Readings, 1981: Spectral characteristics of surface layer turbulence over the sea. *Quart. J. Roy. Meteor. Soc., 107*, 591-614.

Nishiyama, R. T., and A. J. Bedard, 1991: A "Quad-Disc" static pressure probe for measurement of adverse atmospheres: With a comparative review of static pressure probe designs. *Rev. Sci. Instr., 62*, 2193–2204.

Ottersten, H., 1969: Atmospheric structure and radar backscattering in clear air. *Radio Sci., 4*, 1179–1193.

Priestley, J. T., and R. J. Hill, 1985: Measuring high-frequency humidity, temperature and radio refractive index in the surface layer. *J. Atmos. Oceanic Tech., 2*, 235–251.

Readings, C. J., D. A. Haugen, and J. C. Kaimal, 1974: The 1973 Minnesota atmospheric boundary layer experiment. *Weather, 29*, 309–312.

Shaw, R. H., G. E. Kidd, and G. W. Thurtell, 1973: A miniature three-dimensional anemometer for use within and above plant canopies. *Bound.-Layer Meteor., 3*, 359–380.

Strauch, R. G., D. A. Merritt, K. P. Morgan, K. B. Earnshaw, and D. van de Kamp, 1984: The Colorado wind profiling network. *J. Atmos. Oceanic Tech., 1*, 37–49.

Szeicz, G., 1975: Instruments and their exposure. In *Vegetation and the Atmosphere* , Vol. 1 (J. L. Monteith, Ed.), Academic Press, New York, 229-274.

Thomson, D. W., R. L. Coulter, and Z. Warhaft, 1978: Simultaneous measurements of turbulence in the lower atmosphere using sodar and aircraft. *J. Appl. Meteor., 17*, 723–734.

Webb, E. K., G. I. Pearman, and R. Leuning, 1980: Correction of flux measurements for density effects due to heat and water vapor transfer. *Quart. J. Roy. Meteor. Soc., 106*, 85–100.

Wilson, J. D., D. P. Ward, G. W. Thurtell, and G. E. Kidd, 1982: Statistics of atmospheric turbulence within and above a corn canopy. *Bound.-Layer Meteor., 24*, 495–519.

Wucknitz, J., 1980: Flow distortion by supporting structures. In *Air-Sea Interaction—Instruments and Methods.* Plenum Press, New York, 605–626.

Wyngaard, J. C., and S-F. Zhang, 1985: Transducer-shadow effects on turbulence spectra measured by sonic anemometers. *J. Atmos. Oceanic Tech., 2*, 548–558.

Zhang, S. F., J. C. Wyngaard, J. A. Businger, and S. P. Oncley, 1986: Response characteristics of the U.W. sonic anemometer. *J. Atmos. Oceanic Tech., 3*, 315–323.